Tectonophysics 820 (2021) 229114

Contents lists available at ScienceDirect

Tectonophysics

journal homepage: www.elsevier.com/locate/tecto

Seismic structure and composition of the southern central Iberian crust: The ALCUDIA wide angle seismic reflection transect

Imma Palomeras [a,*], Siddique A. Ehsan [b], David J. Martínez Poyatos [c], Puy Ayarza [a], David Martí [d], Ramon Carbonell [d], Antonio Azor [c], Luís M. Parra [e], Ignacio Marzan [d]

[a] Departmento de Geología, Universidad de Salamanca, 37008 Salamanca, Spain
[b] Department of Physics, COMSATS University Islamabad, Lahore Campus, Raiwind Road, Lahore, Pakistan
[c] Departmento de Geodinámica, Facultad de Ciencias, Universidad de Granada, E-18071 Granada, Spain
[d] CSIC-GeoSciences Barcelona (Geo3BCN-CSIC), Lluis Sole i Sabaris s/n, 08028 Barcelona, Spain
[e] Instituto Geológico y Minero de España (IGME), C/ La Calera, 1, 28760 Tres Cantos, Madrid, Spain

ARTICLE INFO

Keywords:
Wide-angle reflection/refraction profile
Central Iberian Zone (Spain)
P- and S-wave velocity model
Poisson's ratio model
Crustal lithologies

ABSTRACT

The nature of the crust beneath central Iberia was estimated by a wide-angle seismic reflection/refraction transect, ALCUDIA-WA, which sampled the southern half of the Variscan Central Iberian Zone, covered in the north by the Cenozoic Tajo Basin. The shot gathers recorded by vertical component sensors revealed well defined P- and S-wave phases. These arrivals were modeled by an iterative forward approach providing 2D crustal models showing variations in the velocity distribution with upper crustal P- and S-wave velocities increasing northwards. The lower crust P-wave velocities are homogeneous along the profile while the S-wave velocities slightly increase northwards. The Moho is placed at 32 km depth in the southern edge of the profile, deepening northward down to 35 km beneath the Tajo Basin. The Poisson's ratio, calculated from P- and S-wave velocities, varies along the profile at upper crustal depths. The highest values are located below the Mora and Pedroches batholiths. These resulting physical properties can serve to constrain the crustal composition by comparing them with laboratory measurements on rock samples. Our results suggest that the upper crust in the southern and central segments of the ALCUDIA profile is made up of low-grade metasedimentary rocks, while the northern segment is dominated by igneous rocks, in agreement with the surface geology. Separated by a sharp boundary located between 12 km (south) and 18 km (north) depth, the lower crust is more homogeneous and shows low Poisson' ratios compatible with a rather felsic composition. However, outstanding lamination described in coincident vertical incidence data indicates some degree of intercalation with mafic components.

1. Introduction

The knowledge of the in-situ physical properties of the Earth's crust is important to study its structure and composition, as well as for understanding its evolution. This knowledge is mostly derived from deep geophysical prospecting, being seismic reflection/refraction surveys the discipline that provides the most reliable and highest-resolution quantitative characterization of the lithosphere.

Normal incidence deep seismic reflection data provide high resolution images of the crust and upper mantle (e.g. BABEL Working Group, 1990; Knapp et al., 1996; MONA LISA Working Group, 1997; Cook et al., 1999, 2004; Simancas et al., 2003; Ayarza et al., 2004; Martínez Poyatos et al., 2012) revealing complex internal structures and reflectivity fabrics. Additionally, controlled source wide-angle seismic reflection/refraction experiments are the main source of information about seismic-wave velocities in the lithosphere (e.g. Ayarza et al., 1998; Carbonell, 2004; Carbonell et al., 2000; Palomeras et al., 2011, 2009; Ruiz et al., 2017). By comparing the resulting seismic velocities from controlled source experiments with measurements done in laboratories using rock samples (Hawman et al., 1990; Palomeras et al., 2009; Shillington et al., 2004) we can estimate the composition of the lithosphere. Usually only P-wave velocity models are derived from wide-angle experiments. Nevertheless, in the case of crystalline rocks, for a given P-wave velocity the range of rock types is not narrow, hindering the identification of lithologies (Birch, 1961, 1960; Christensen and Mooney, 1995; Rudnick and Fountain, 1995). In this regard, S-wave

* Corresponding author.
E-mail address: imma@usal.es (I. Palomeras).

https://doi.org/10.1016/j.tecto.2021.229114
Received 5 November 2020; Received in revised form 5 October 2021; Accepted 17 October 2021
Available online 23 October 2021

velocities provide additional constraints that helps to untangle the correlations between indirectly measured velocities and rock types (lithologies). Furthermore, the Poisson's or Vp/Vs ratio is also an additional constraints on crustal composition.

Within the Variscan Massif in Spain (Fig. 1), the southern Central Iberian Zone (CIZ) is characterized by Late Paleozoic upright folds and granite intrusions (e.g. Azor et al., 2019; Pérez-Estaún and Bea, 2004), with no exposures of deep seated lithologies. It is, thus, important to come up with techniques that help us to image the deep crust in order to address its structure and composition, and if possible, the processes involved in deformation. In this regard, the multichannel ALCUDIA normal incidence (ALCUDIA-NI) seismic reflection profile (Fig. 1) provided a detailed image of the crustal structure of the southern CIZ far from the suture units (Ehsan et al., 2014; Martínez Poyatos et al., 2012). Later on, in spring 2012 the ALCUDIA wide-angle (ALCUDIA-WA) (Ehsan et al., 2015) seismic reflection/refraction data were acquired to place key constraints on the seismic velocities of this old intracontinental orogenic region (Fig. 1). Ehsan et al. (2015) analyzed the P-wave arrivals and from the resulting model, they proposed a crustal composition for the southern CIZ.

Nevertheless, including additional constraints like those provided by the S-wave velocities and Poisson's ratios, decrease the range of possible lithologies leading to a more reliable compositional crustal model. In this article we reevaluate the P-wave velocity model (Ehsan et al., 2015) and present the S-wave response of the ALCUDIA-WA seismic reflection/refraction transect (Fig. 1). The data show strong and laterally continuous P-wave arrivals, and although recorded with vertical single component sensors, it also presents high-amplitude S-wave phases. The analysis of these phases allow to decipher the distribution of both P- and S-wave velocities in the crust of this area. With the resulting velocities the Poisson's ratio has been calculated. All these physical properties, jointly with densities obtained from gravity modeling (Ehsan et al., 2015) are used to further constraint the crustal composition of this internal area of the Iberian Massif, and to shed light on its evolution.

Accordingly, the ALCUDIA-WA dataset has allowed to: (1) derive well resolved P- and S-wave velocity models, (2) estimate, where possible, Poisson's ratios from those calculated velocities, (3) derive the most likely crustal lithologies, and (4) foster new insights into the large scale structures and tectonic evolution of the Variscan belt of western Europe.

2. Geological setting and geophysical background

2.1. Geological setting

The Variscan Orogen was built during the Late Paleozoic from the collision between two continents, Laurentia/Baltica and Gondwana (e.g. Franke, 2000; Matte, 2001, 1986). The Iberian Massif (Fig. 1), which occupies a significant part of the Iberian Peninsula, is the major exposure of this orogen in southern Europe. This massif has been classically divided into six zones (Fig. 1): the Western Asturian-Leonese Zone (WALZ), the Galicia-Tras-os-Montes Zone (GTMZ), the CIZ, and the Ossa-Morena Zone (OMZ) represent the internal zones, whereas the Cantabrian Zone (CZ) and the South Portuguese Zone (SPZ) represent the external zones (Pérez-Estaún and Bea, 2004; Simancas, 2019, and references therein).

The CIZ constitutes a major portion of the Iberian Massif. Its southern transect is characterized by limited offset faults, upright folds, and a variety of plutonic bodies (Azor et al., 2019; Martínez Catalán et al., 2004). The Badajoz–Cordoba Shear Zone (BCSZ) is the boundary between the CIZ and OMZ (Fig. 1) and attests a suture contact of the orogen (Azor et al., 2019, 1994; Burg et al., 1981; Simancas et al., 2001). This ~5 km-thick cartographic band consists of exhumed high-grade metasediments orthogneisses, and amphibolites, intensely shared and metamorphosed during the Variscan Orogeny (Azor et al., 1994; Burg et al., 1981; Gómez-Pugnaire et al., 2003; López Sánchez-Vizcaíno et al., 2003; Ordoñez Casado, 1998). The Matachel and Azuaga faults bound the BCSZ to the north and south, respectively, further evidencing its general dip towards the northeast (Simancas et al., 2003).

The stratigraphic succession of the southernmost CIZ starts with the Serie Negra (Fig. 1). This late Neoproterozoic Formation consists of graphite-rich schists, slates, metagreywackes, quartzites, and amphibolites. The Alcudian succession (Vendian to Lower Cambrian), cropping out to the north consists of low-grade slates and greywackes with conglomerates. All these rocks are overlaid by an Ordovician to Devonian shallow-marine siliciclastic succession composed of alternating quarzitic and slaty beds. Finally, the Lower Carboniferous consists of slates and greywackes with basaltic intercalations. Moreover, the surface geology of the studied transect of the CIZ features granitic plutons (more abundant and accompanied by anatectic complexes towards the north), and a series of upright synclinal and anticlinal structures of different sizes developed at low-grade metamorphic conditions (Fig. 1) (Martínez Poyatos et al., 2012).

The Spanish Central System (CS), an Alpine mountain range with a linear ENE-WSW trend, bounds the Cenozoic Tajo Basin (TB) to the north (Fig. 1), while the Toledo Mountains represent its southern boundary. The TB attests a continuous sedimentary record from the Late Cretaceous up to the Upper Miocene (Alonso-Zarza et al., 2004; de Vicente and Muñoz-Martín, 2013). The basin, with a total sediment thickness of ~2000 m in its southwestern margin (de Vicente and Muñoz-Martín, 2013), features a broad range of lithologies (conglomerates, sandstones, clays, marls, limestones, and gypsums).

2.2. Geophysical background

The nature of the lithosphere of the southern Iberian Massif has been of interest since the early 1990s (e.g. Ehsan et al., 2015; Flecha et al., 2009; Iliha DSS Group, 1993; Martínez Poyatos et al., 2012; Monteiro Santos et al., 1999; Palomeras et al., 2009; Pous et al., 2004, 2011; Simancas et al., 2003). These experiments sampled the SPZ, the OMZ, and the CIZ (Fig. 1). Two of them, namely IBERSEIS and ALCUDIA, consisted of controlled source multiseismic initiatives that included normal incidence and wide-angle reflection/refraction seismic data. Together, they delineate the structure and physical properties of the lithosphere of the southern Iberian Massif along a ~ 600 km transect (Ehsan et al., 2015, 2014; Flecha et al., 2009; Martínez Poyatos et al., 2012; Palomeras et al., 2011, 2009; Simancas et al., 2013).

The IBERSEIS experiment included a normal incidence profile (Simancas et al., 2003) and two deep seismic reflection/refraction wide-angle transects (Palomeras et al., 2009) (Fig. 1). The results improved our knowledge about the crustal and lithospheric architecture across the tectonic zones and suture units through the southern Iberian Massif. Besides a detailed image provided by the normal incidence experiment (Simancas et al., 2003), the wide-angle profiles provided P- and S-wave velocity models and thus the Poisson's ratio distribution on the crust (Palomeras et al., 2011, 2009). The IBERSEIS profiles showed a differentiated upper and lower crust, as well as high reflectivity, velocity, and Poisson's ratio bodies at midcrustal depths interpreted as mafic intrusions of early Carboniferous age. The inferred lithologies for the upper crust included metagraywackes, granites, and gneisses. The middle crustal high velocity and Poisson's ratio bodies are compatible with amphibolites, gabbros, mafic granulite, and metabasalt. The lower crustal possible composition includes amphibolite and meta-basalts.The ALCUDIA-NI survey imaged the southern CIZ and its boundary with the OMZ providing a detailed image of the crust and uppermost mantle. Several common features are observed in both the IBERSEIS and ALCUDIA normal incidence transects (Fig. 1): (1) varying reflectivity in the upper crust matching the surface geology; (2) upper and lower crustal reflectivity merges in a decoupling zone; (3) highly reflective fabric in the BCSZ; (4) relatively large number of prominent reflections and evidences of crocodile type collision fabric in the lower crust between the OMZ and the CIZ; (5) pristine Moho discontinuity located at

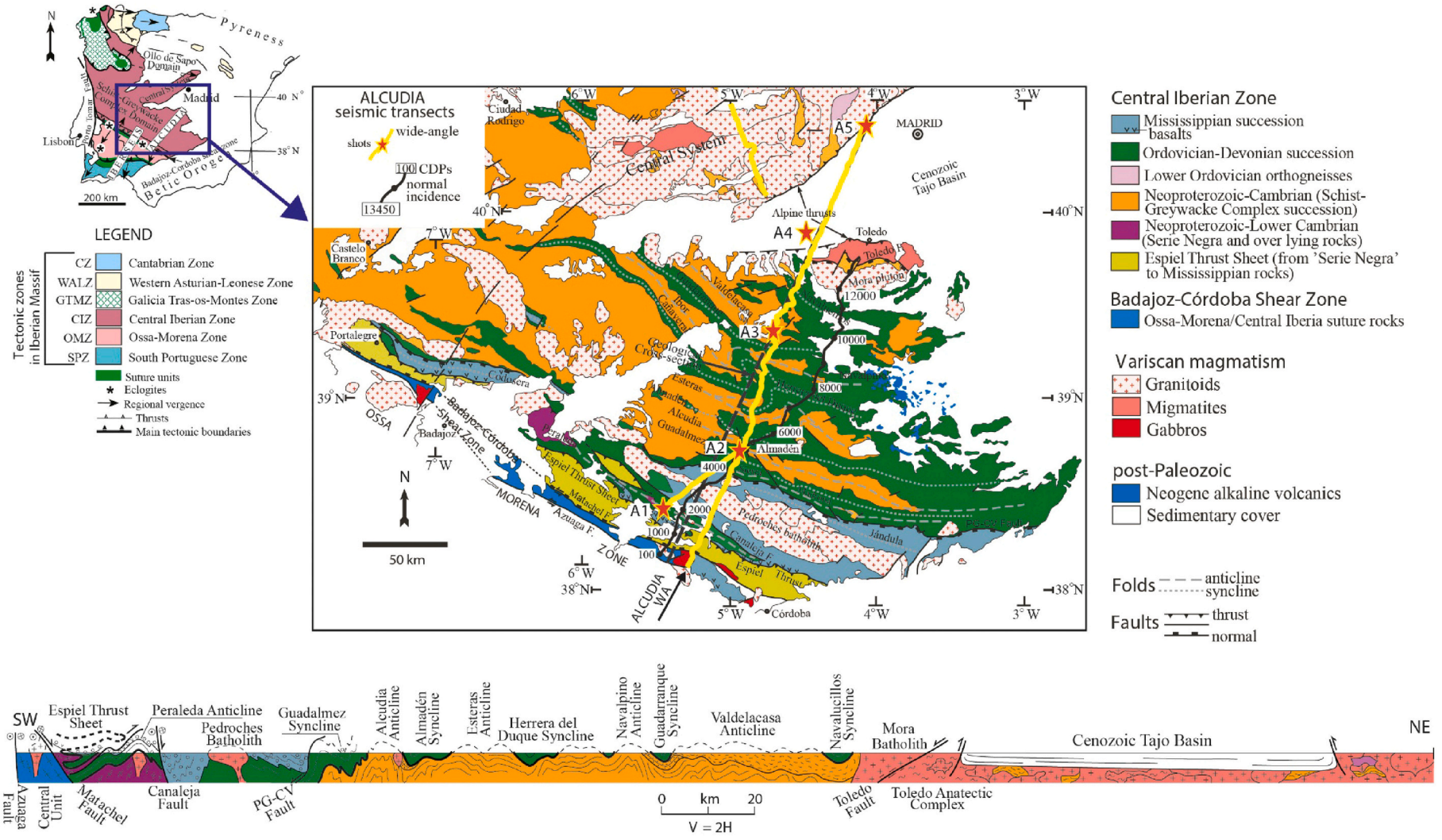

Fig. 1. Map of the main tectonic zones of the Variscan Iberian Massif (top left). The location of normal incidence and wide-angle profiles (IBERSEIS and ALCUDIA) is shown over the tectonic map. The study area is highlighted by a blue rectangle. Main panel: Geological map of the study area. The ALCUDIA-NI transect is highlighted by a thick black line. The layout of the ALCUDIA-WA transect with five shots (A1–A5) is shown over the map as a yellow line and red stars, respectively. Bottom: Geological cross section constructed from surface information collected in the field along the dash gray line marked on the map. Geological map modified after Martínez Poyatos et al. (2012).

10–11 s two-way travel-time (twtt), and (6) scarcely reflective upper mantle. Both datasets also imaged a sharp change in reflectivity from a high amplitude reflectivity fabric in the lower crust to an almost transparent mantle (Martínez Poyatos et al., 2012; Simancas et al., 2003).

The ALCUDIA-WA profile provided the first detailed P-wave velocity model beneath the southern CIZ (Ehsan et al., 2015). These velocities were compared with those of the different rock types measured in the laboratory under high temperature and pressure conditions, providing initial constraints on the composition of the crust along the CIZ and the TB. The outcropping rocks compatible with the velocity model are granites, granodiorites, slates, greywackes, schists, gneisses, sandstones, limestones, and quartzites. The lower crust P-wave velocities are consistent with amphibolite, diabase, mafic granulites, gabbros, schists, and gneisses.

The area has also been studied by nearly coincident gravity and magnetotelluric (MT) studies (Ehsan et al., 2015; García-Lobón et al., 2014; Pous et al., 2011), revealing a mild but persistent conductive lower crust and a variety of conductive and resistive bodies in the upper crust (Pous et al., 2011).

3. The ALCUDIA wide-angle seismic reflection profile

3.1. Acquisition

The ALCUDIA-WA seismic reflection data, collected in early May 2012 consisted of a ~ 300 km-long transect which covers the area extending from the BCSZ (the northern boundary of the OMZ) to the southern boundary of the CS, across the CIZ and the TB, with a NE-SW orientation (Fig. 1). A total of ~900 vertical component autonomous digital recording seismic stations (TEXANS) from the IRIS-PASSCAL Instrument Pool were deployed along the line with a nominal spacing of 400 m. The impulse source signal was achieved by using 1TM of explosives fired in single 50–60 m deep boreholes. A total of 5 shots were fired distributed along the line with a nominal spacing of 70 km. The acquisition parameters are listed in Table 1, and further details are given in Ehsan et al. (2015). Shot A1 is ~20 km offline (Fig. 1) and has been excluded of our analysis due to its acquisition geometry, since it can introduce travel-time complexities and uncertainties in the quantitative interpretation. Therefore, we have examined four shot records (A2-A5) (Fig. 1), with the aim of analyzing their P- and S-wave information.

3.2. Processing

The processing of the ALCUDIA-WA shot gathers involved (i) amplitude corrections for spherical spreading (amplitude recovery, scaling), (ii) amplitude balancing, (iii) band-pass filtering, and, (iv) deconvolution. The processing flow cleaned up the shot gathers, preserving the true amplitudes, and increasing the signal-to-noise ratio. For the P-wave analysis, the processing parameters were detailed in Ehsan et al. (2015). Here we describe the processing parameters used to enhance the S-wave arrivals.

The band pass filter parameters were picked after a frequency analysis (Fig. 2). The main phases feature a frequency range from 4 to 20 Hz, with the highest amplitudes at frequencies about 8–14 Hz for the most prominent S-wave phases. Accordingly, a band-pass filter between 5 and 20 Hz (2–5–20-25 Hz) was applied to enhance the coherency of seismic events. Filtering eased the interpretation of data and also helped to attenuate source-generated noise and surface waves. Finally, the frequency content was whitened applying predictive Wiener deconvolution which sharpened the source signal.

The processing flow significantly improved the resolution of the shot records (Fig. 3). They show variations in the seismic signature, which are primarily representative of the internal geological/lithological structure. A reduction velocity of 4.6 km/s ($8/3^{1/2}$), which enhances deep crustal and mantle phases is used to display the shot gathers.

Table 1
Data acquisition parameters for ALCUDIA-WA transect.

Survey parameters	
Type of survey	2D crooked line
Recording system	IRIS-TEXANS (RT125A)
Nominal spread	Asymmetrical split spread
Source type	Chemical explosive
Nominal shot depth	50–60 m
Nominal shot interval	60–80 km
Nominal shot size	1000 Kg
Shot design	Single borehole
Total No. of shots	5 (1 TM each)
Geophones	Single component, 10 Hz
Nominal active channels	1000
Nominal receiver interval	340–600 m
Recording length	80 s
Total length	350 km
Date acquired	01/05–15/05, 2012

3.3. Data description

The processed shot records provide continuous coverage at all offsets (from 0 to ~300 km) featuring excellent lateral continuity of the seismic arrivals (Figs. 3 and 4). A critical element for interpretation and velocity modeling is the phase identification and travel-time picking. Different phase arrivals have been identified and correlated from shot to shot. The P-wave phase identification (Fig. 3) was already presented by Ehsan et al. (2015) and here it has been improved. The different arrivals were labeled following the conventional notation used in refraction experiments, Ps (P-wave traveling through the sediments), Pg (direct arrivals P-wave arrivals through the basement), PcP (intra-crustal P-wave reflection), PmP (P-wave energy reflected at the base of the crust), and Pn (P head wave traveling within the upper mantle).

The S-wave arrivals with similar amplitude and zero offset travel-times were given the same name (Fig. 4). The identified and picked phases have been labeled accordingly following also the conventional notation used in wide-angle reflection/refraction surveys: (1) Ss for the S-wave traveling through sediments, (2) Sg for the direct S-wave traveling through the basement, (3) SmS for the S-waves reflected at the Moho discontinuity emerging as a S-wave; (4) PmP for the reflection of the P-wave at the Moho emerging as a P-wave, and (5) PmS/SmP for the P-wave reflected off the Moho discontinuity as a S-wave or vice versa (converted waves). The critical refraction at the Moho boundary through the upper mantle (Sn) is difficult to identify, thus preventing the modeling of subcrustal S-wave velocities. Ahead, only S-wave phases are described although P-wave arrivals are also identified in Fig. 4.

A strong Sg phase is identifiable as first S-wave arrival up to ~45 km at positive and negative offsets on shot gather A2 (Fig. 4a). A decrease in its amplitude is evident beyond these offsets. At negative offsets, the SmS phase is relatively weak although it can be identified at 12 s reduced travel-time. For the positive offsets, the SmS phase is identified from 70 km offset as a broad reflective ~2 s-long band at 11 s reduced travel-time.

Shot record A3 (Fig. 4b) reveals clear, high-amplitude S-wave arrivals. The Sg phase can be followed at all negative offsets and up to 80 km offset at the positive branch. A high amplitude SmS phase is observed from −80 km to −130 km offset and from +60 km to +120 km offsets at ~11 s reduced travel-time. In both cases, the SmS phase shows a ~ 1.5 s coda.

In shot record A4 (Fig. 4c), clear direct S-wave arrivals (Sg) are seen at all negative offsets. This arrival presents a high amplitude up to −60 km offset, decreasing beyond this offset. At positive offsets, the Sg is only identifiable at low offsets, up to ~15 km, as a sharp strong arrival. The SmS phase features high amplitudes from −60 km to −120 km offset at ~11 s reduced travel-time. The northern branch of shot A4 is less reflective and features shorter offsets (~65 km), and thus no SmS can be identified.

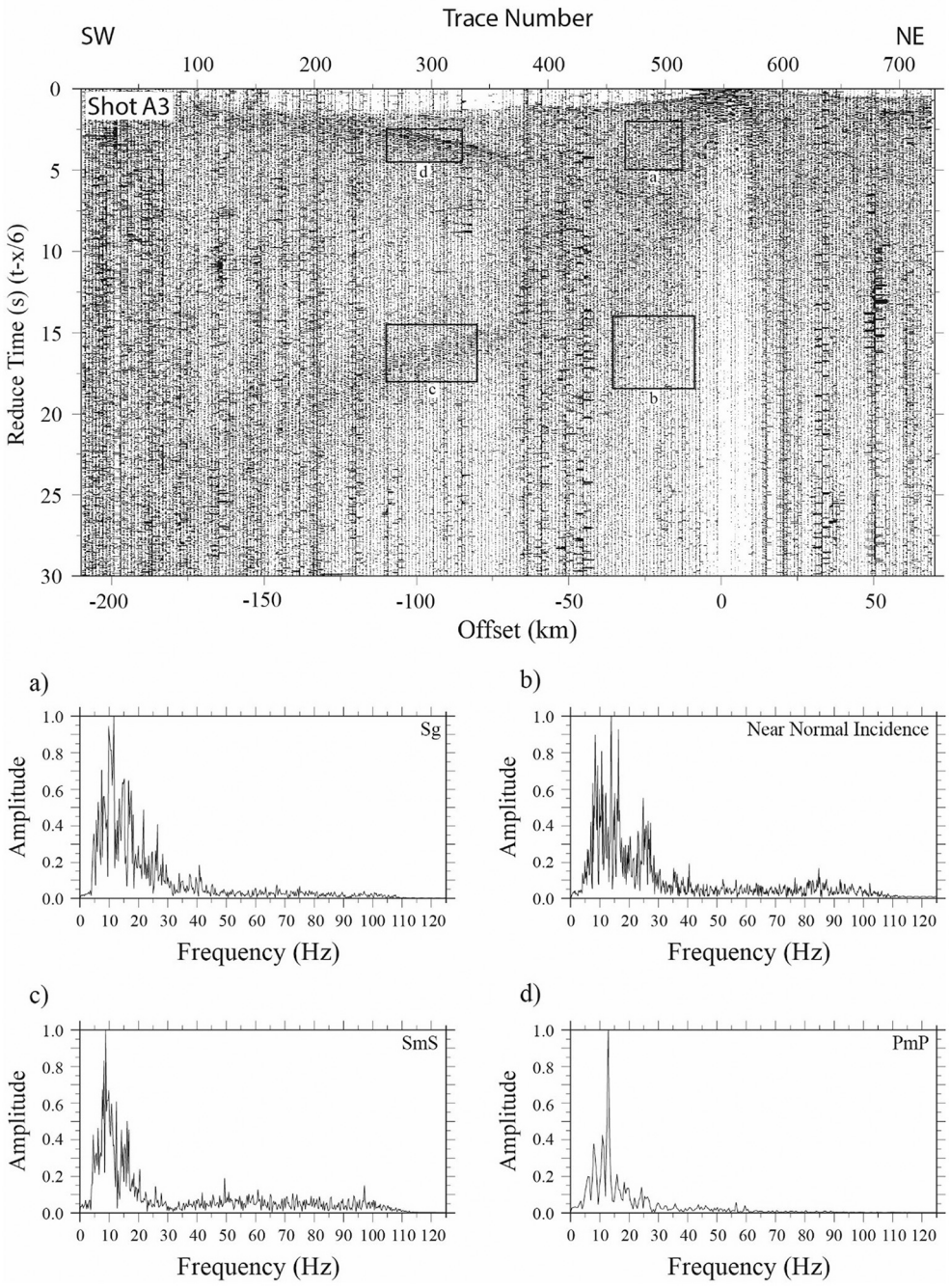

Fig. 2. (a) Raw shot gather A4 displayed with a reduction velocity of 6.0 km/s. (i), (ii), (iii) and (iv) Amplitude spectra of the main seismic phases (Sg, SmS and PmP) calculated over the highlighted windows in the raw shot gather A4. The seismic phases show high amplitudes up to frequencies of 20 Hz. (b) Processed shot gather A4 displayed with a reduction velocity of 6.0 km/s. The processing allowed to enhance the lateral coherency of the main seismic reflections (Sg, SmS and PmP) indicated by black arrows.

Shot record A5 (Fig. 4d) features high amplitude P-waves traveling through the TB sediments which interferes with the S-waves traveling through basin infill. Unfortunately, the Ss phases cannot be identified, hindering the calculation of S-wave velocities for the TB. Contrarily, the Sg phase is clearly identified between −12 to −25 km offsets as a sharp high amplitude arrival. At larger offsets, the first S-wave arrivals are hidden by the P-wave energy, but the Sg is again recognized as a weak arrival from −70 km and beyond. The SmS phase is imaged as a simple wavelet, ~1.0 s long, at −80 km offsets, and 11.5 s at reduced travel time. The SmS phase in this shot presents a weak reflectivity that can be traced up to −150 km offset.

The converted reflected wave at the Moho (PmP/SmP) is also recognized on all shot gathers with an intercept time of ~14–15 s (Fig. 3).

4. Modeling

2D P- and S-wave velocity models have been obtained using an iterative forward modeling approach by trial and error ray tracing methodology (Zelt and Smith, 1992). The 2D ray-tracing technique requires defining a reference transect. Therefore, the first step was to project the source and receiver locations onto the reference line in order to preserve the offset information. Then, the velocities and boundaries of an initial layered model were modified in order to achieve the better fit between the observed and modeled arrival times (Zelt and Smith, 1992).

We firstly re-evaluated the existing P-wave velocity model. A more accurate P-wave phase picking, primarily at short offsets, produced a slightly different model (Fig. 5b) than the one presented by Ehsan et al. (2015).

Later on, we undertook S-wave modeling. The laterally limited

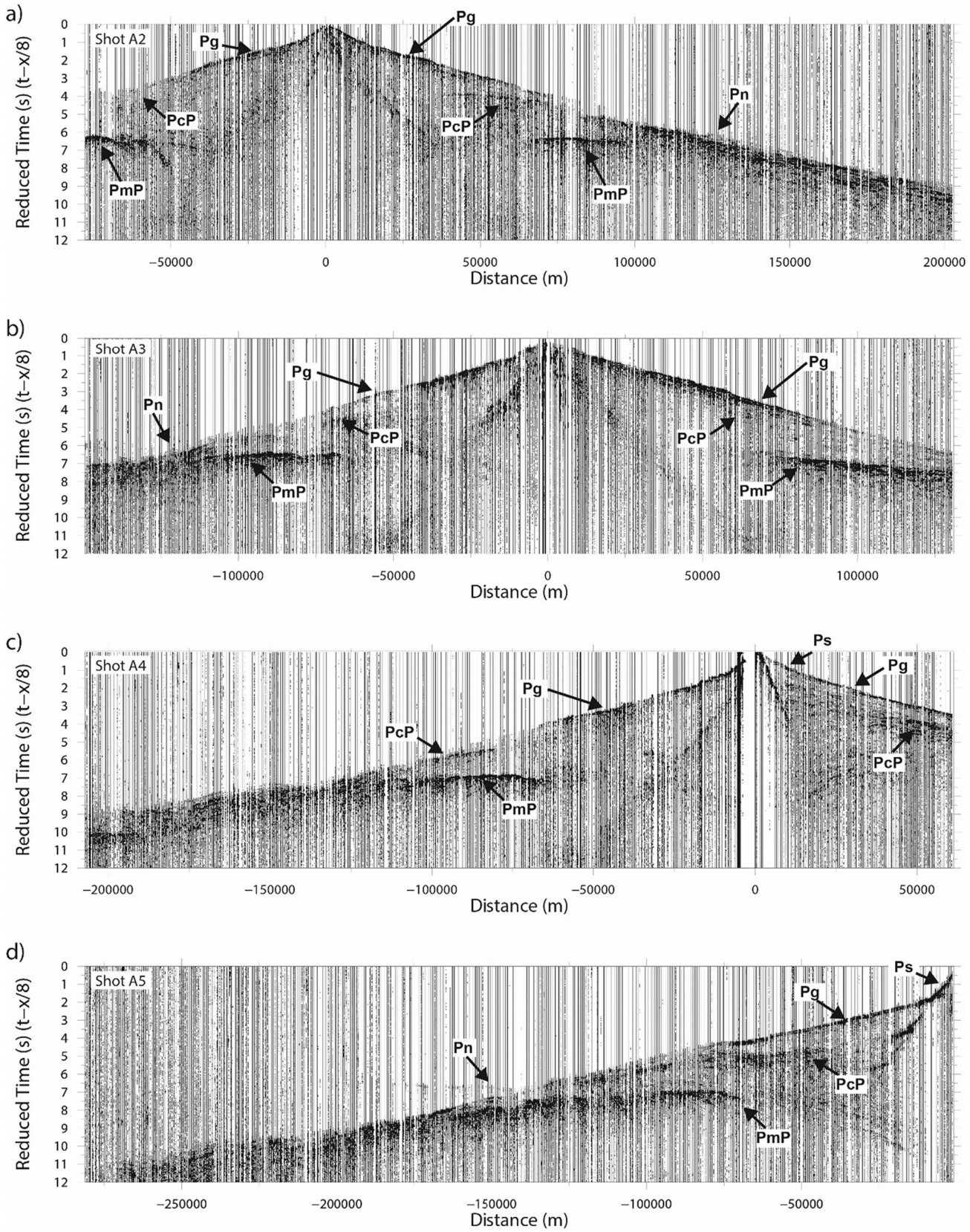

Fig. 3. (a), (b), (c) and (d) From south to north, the four shot gathers (A2-A5) displayed with a reduction velocity of 8.0 km/s, across the ALCUDIA-WA transect. Positive offsets are located to the north of the source location, and negative offsets are considered to be located to the south of the source location. A band-pass filter of 5–20 Hz was applied in order to enhance the reflectivity of the P-wave arrivals. Pg is the first P-wave arrival, PcP is a P-wave reflected at the base of the upper crust, PmP is a P-wave reflected from the crust-mantle discontinuity.

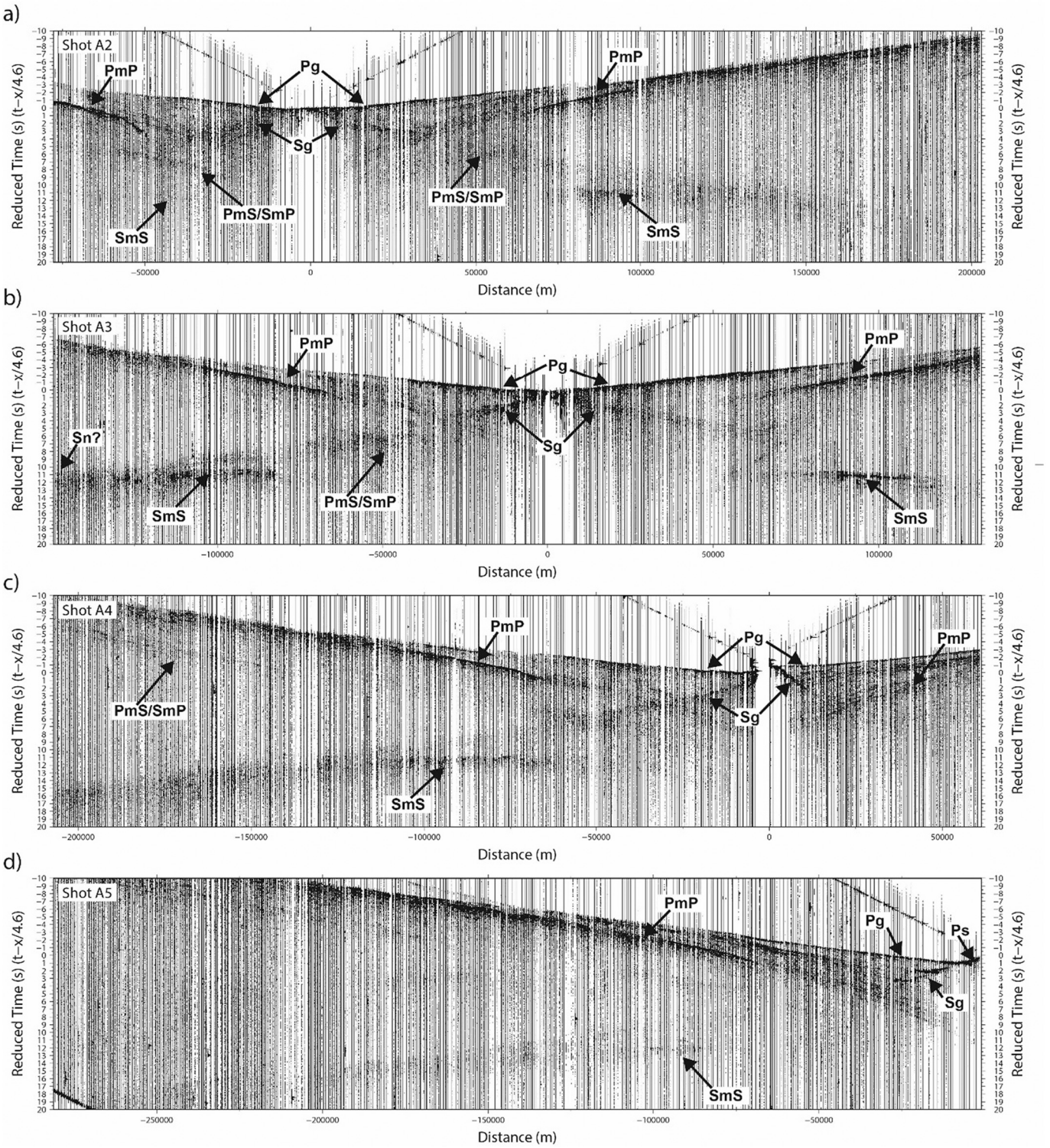

Fig. 4. (a), (b), (c) and (d) From south to north, the four shot gathers (A2–A5) displayed with a reduction velocity of 4.6 km/s, across the ALCUDIA-WA transect. Positive offsets are located to the north of the source location, and negative offsets are considered to be located to the south of the source location. A band-pass filter of 5–20 Hz was applied in order to enhance the reflectivity of the S-wave arrivals. Sg is the first S-wave arrival, SmS is a S-wave reflected from the crust-mantle, PmS /SmP is the P wave incident at the Moho discontinuity and converted to a reflected S-wave or vice versa (converted waves).

reflectivity of S-wave main phases (e.g., SmS, Fig. 4) and the travel-time, amplitude, and waveform variations of the Sg phase evidence the seismic complexity of the upper crust. Shot gathers feature prominent intracrustal reflected (e.g., PcP) and subcrustal refracted (Pn) P-wave phases (Fig. 3), while no intracrustal reflected and subcrustal refracted S-wave phases (Sn) have been observed. Accordingly, the structure of the S-wave model relies on the P-wave results at these levels (Fig. 5b).

The initial S-wave velocity distribution was derived from the P-wave velocities using a Vp/Vs ratio of1.73, which assumes a Poisson's ratio of 0.25. As a second step, the crustal boundaries provided by the P-wave modeling were kept, whereas the S-wave velocities were varied to adjust the picked phases. The resulting S-wave velocity model is presented in

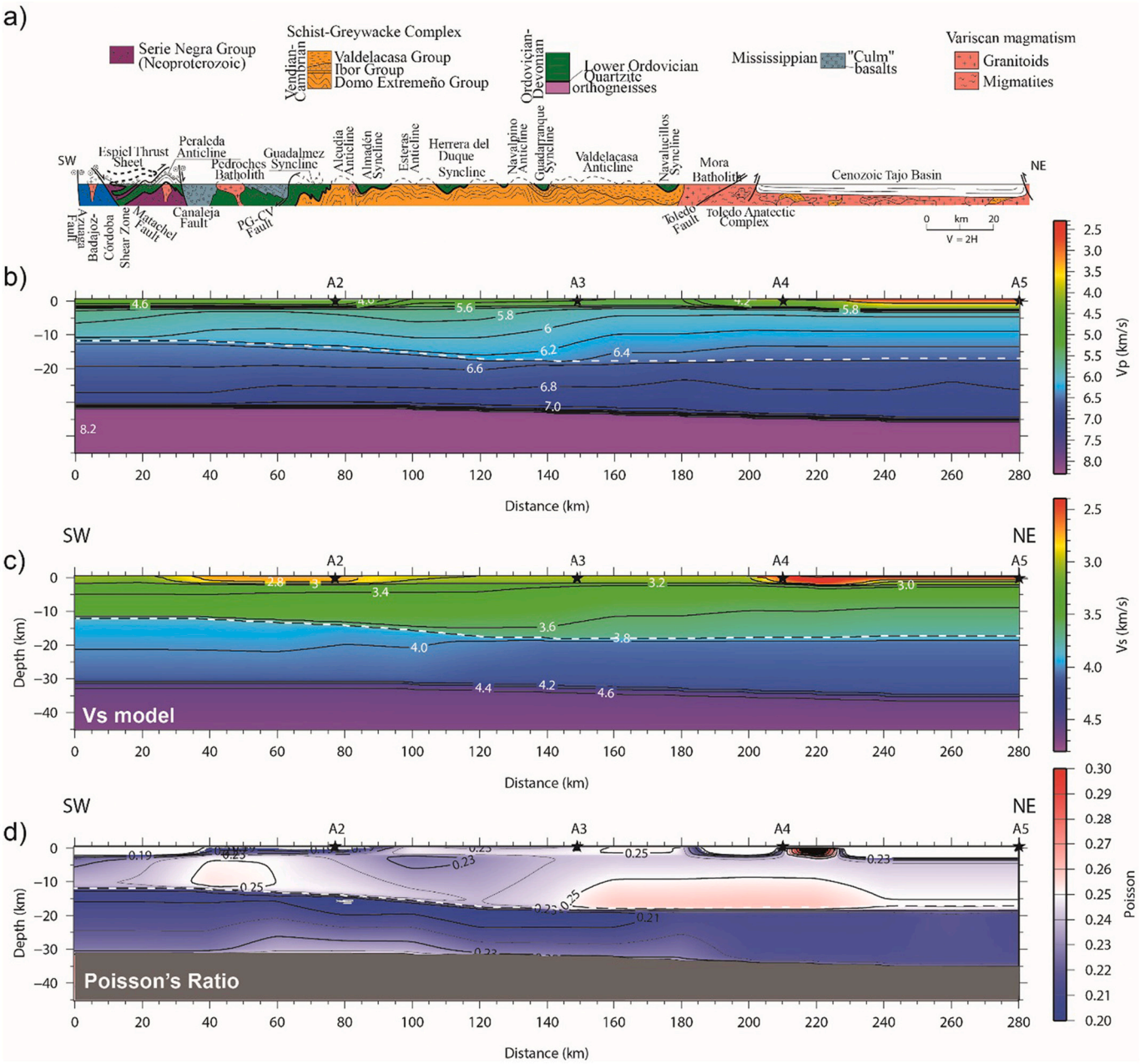

Fig. 5. (a) Generalized geological cross section along the ALCUDIA-WA transect. (b) Crustal P-wave velocity model computed along the ALCUDIA-WA transect. (c) S-wave velocity model obtained by iterative ray tracing technique along the ALCUDIA-WA transect. (d) Poisson's ratio model derived from the P- and S-wave velocity models. The black stars represent the shot positions. White dashed line marks the upper to lower crust discontinuity.

Fig. 5c. The upper crustal velocities are constrained by the Sg phase which is identified in the shot gathers at large offsets (greater than 80 km, Fig. 4). The lower crustal velocities are adjusted by the SmS phase. Since no Sn phase is recognized, it is not possible to model S-wave velocities below the Moho. A good fit between calculated and identified travel times exists and is shown in Figs. 6 and 7 for the P- and S-wave arrivals, respectively.

For an isotropic medium, the Poisson's Ratio (σ) is defined as:

$$\sigma = \frac{1}{2}\left[1 - \frac{1}{\left(\frac{V_p}{V_s}\right)^2 - 1}\right]$$

Accordingly, a Poisson's ratio model (Fig. 5d) has been computed from the P- and S-wave velocity models presented in this work.

5. Results: 2D P- and S-wave seismic velocity and Poisson's Ratio models

The new P-wave velocity model (Fig. 5b) distinguishes an uppermost crustal layer (up to ~2-km depth) with lower P-wave velocities than the ones obtained by Ehsan et al. (2015). Below this thin layer, the new model maintains the structure obtained by these authors, although with slightly higher average upper crustal velocities (0.1–0.2 km/s). The major difference is observed in the upper crust (below 2 km) between km 150 and 210, where velocities are up to 0.35 km/s higher in the new model. This area is coincident with the Mora granitic batholith and the Toledo migmatites, and, therefore, new calculated velocities of 6.0–6.2 km/s seem reasonable. The prominent middle crustal reflection (PcP) indicates a noticeable change on the physical properties between the upper and lower crust. This discontinuity is placed at 12 km-depth in the

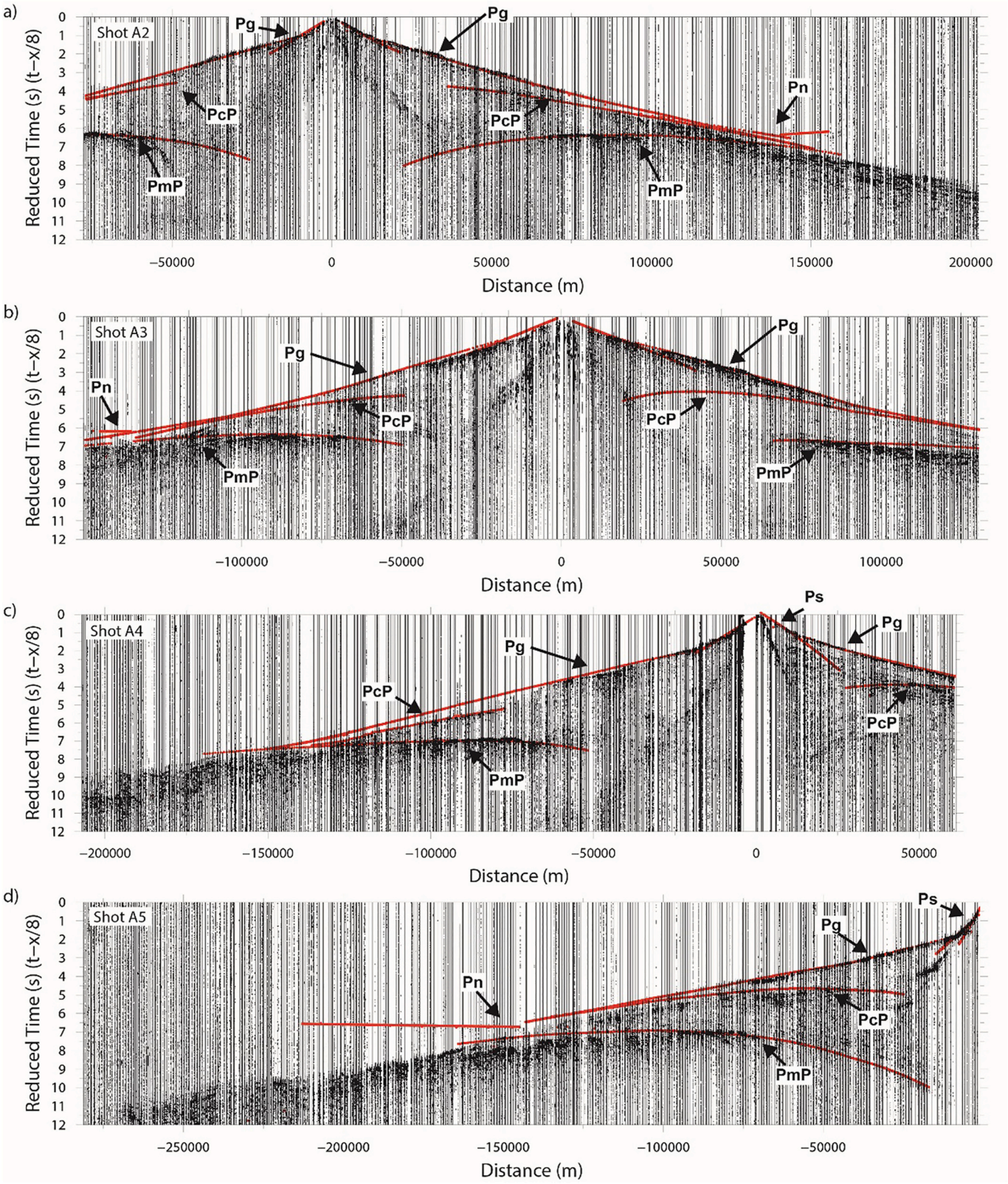

Fig. 6. The theoretical traveltime branches predicted by the P-wave velocity model generated by the Zelt and Smith [1992] algorithm, in order to illustrate the agreement between the observed phases and the model prediction (red lines). The data have the same processing as in Fig. 3 and a reduction velocity of 8.0 km/s is used to display shot gathers (A2-A5).

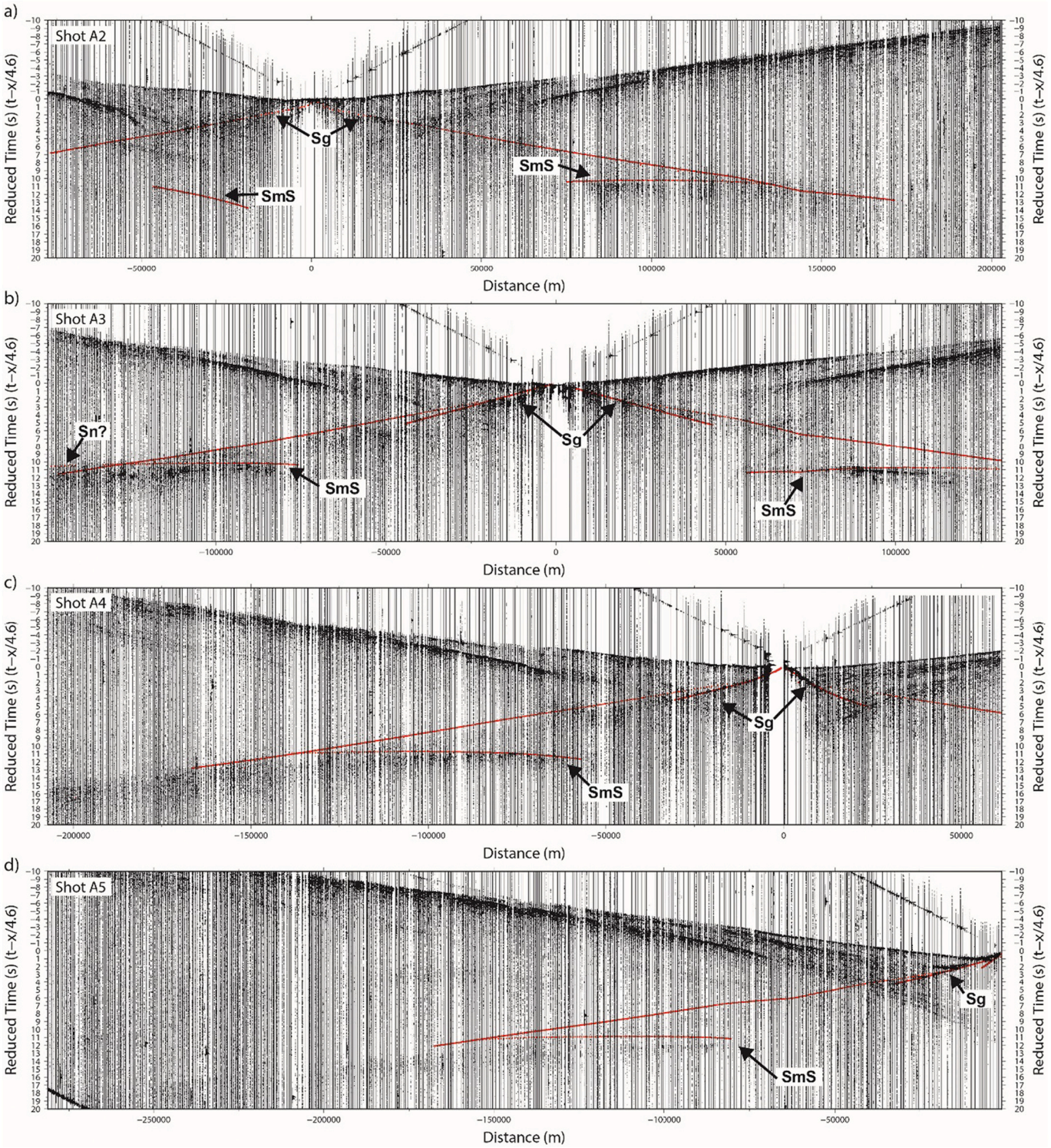

Fig. 7. The theoretical traveltime branches predicted by the S-wave velocity model generated by the Zelt and Smith [1992] algorithm, in order to illustrate the agreement between the observed phases and the model prediction (red lines). The data have the same processing as in Fig. 4 and a reduction velocity of 4.6 km/s is used to display shot gathers (A2-A5).

southern edge, deepening to the north down to 18 km beneath the TB. The northward thickening of the upper crust was already imaged by the ALCUDIA-NI seismic profile (Martínez Poyatos et al., 2012), which provided a fairly clear image of the geometry of this mid-crustal boundary. The lower crust velocities are laterally homogeneous along the profile increasing with depth from 6.6 to 7.0 km/s. The Pn phase constraints the Moho interface position at 32 km depth on the southern part of the profile, deepening down to 35 km northwards.

The resulting S-wave velocity model (Fig. 5c) shows a distribution of values that varies laterally along the transect, especially at the shallowest ~2 km. At these depths, two low-velocity zones (LVZ) are modeled. The southern LVZ (Vs ~ 2.85 km/s), located between 30 and 90 km along the line, coincides with outcrops of diverse low-grade metasedimentary rocks (with preponderance of quartzites) and

granites. Intense fracturing of these competent but otherwise low velocity lithologies could account for the low velocities observed. A second LVZ (~2.50 km/s) is observed from km 200 to the northern end of the line, coincident with the TB. It must be stressed that the low P-wave velocities on the basin mask the Ss phase, which cannot be picked on shot gathers A4 and A5 (Fig. 3c and d). Therefore, the S-wave velocity for the basin has been modeled by taking a constant Vp/Vs = 1.76. This value seems reasonable for thick sedimentary basins (e.g. Zhao et al., 2013). Due to the too poor constraints on the S-wave velocity at the TB, we will not interpret either the S-wave velocity model or the Poisson's ratio in this part of the transect.

The prominent Sg phase observed up to long offsets in all shot gathers allow us to model the upper crust S-wave velocities. As inferred above, the modeled upper crust extends down to 12 km at the southern edge of the profile, increasing to 18 km-depth northwards. To the south, upper crustal S-wave velocities vary from 3.2 km/s at ~2 km-depth to 3.6 km/s at the upper-lower crust boundary. North of km ~150, upper crustal velocities increase with depth from 3.4 km/s to 3.8 km/s. This lateral change on S-wave velocity may represent the depth expression of the lithological change observed in the surface exposures, i.e. preponderance of igneous and high-grade metamorphic rocks (excluding the TB) in the northern part of the profile.

The lower crust S-wave velocity model indicates slightly higher velocities at the northern part of the profile compared to the southernmost ~100 km. To the south, Vs varies with depth from 3.8 km/s to 4.2 km/s. To the north the velocities are more homogeneous increasing from 4.0 km/s at 18 km-depth to 4.2 km/s at the base of the crust. This lateral velocity change in the lower crust is not observed on the P-wave velocity model, thus indicating that whatever the cause of the S-wave velocity variations, it does not affect the P-wave velocities. The high-amplitude SmS phase indicates a sharp increase in Vs at the base of the crust. However, due to the lack of Sn phases, the uppermost mantle S-wave velocity cannot be constrained.

The Poisson's ratios show clear differences between the upper and lower crust of the southern CIZ, as well as lateral variations along the profile, especially in the upper crust (Fig. 5d). Thus, the upper crust Poisson's ratio from km 0 to km ~80 along the line is ~0.25, while north of shot point A2 the values decrease to 0.24–0.23 from 80 km to 140 km along the line. A higher Poisson's ratio region is imaged between 140 km and 240 km along the line from 5 km-depth to the base of the upper crust. The maximum values (~0.26) could be related to igneous processes affecting the upper crust and evidenced by the existence of the Mora batholith and the Toledo Anatectic complex, which crop out south of shot A4. In general, the low Poisson's ratios (less than 0.25) featured between shot A2 and A3 are in good agreement with those obtained by Palomeras et al. (2011) for the same area (the IBERSEIS-WA profile northern edge coincides with shot A2), except locally in the middle crust, where the IBERSEIS profiles imaged a high P-wave velocity and Poisson's ratio body related to a mafic intrusion. Such a high velocity body is not imaged in the ALCUDIA profile, indicating that this feature is limited to the OMZ.

In the southern part of the profile, the lower crust from ~13–20 km-depth down to the Moho, is quite homogeneous and features Poisson's ratio values around 0.22–0.23.

5.1. Model resolution and uncertainties

The good agreement (<0.4 s and similar slopes/trends) between the theoretical travel times predicted by the P- and S-wave velocity model and the observed phases (Pg, PcP, and PmP for the P waves, and Sg and SmS for the S waves) is presented in Figs. 6 and 7. One of the factors that contributed to the small mismatch between the observed and modeled travel-times is the acquisition geometry. Although the crooked line geometry of the ALCUDIA-WA transect followed roads and paths, its design define an almost straight line perpendicular to the strike of major regional structures. Since the velocity-depth models are based on a straight 2D interpretation approach, the procedure of projecting the recorded 3-D crooked line to a 2-D setup affects the true locations of the receivers, although not substantially. Therefore, no noticeable errors are introduced in the modeled travel-times although deep phases (e.g. PmP) and long offsets may perform noticeable misfits.

The uncertainties of the models are estimated from the fit between modeled and observed travel-times. The maximum observed mismatch is $<\pm 0.2$ s and $< \pm 0.4$ s for the P- and S-wave travel-times, respectively (Figs. 6 and 7). We have estimated the uncertainty in both, velocity and depth using trial and error modeling. The resulting errors corresponding to these uncertainties are $\leqslant \pm$ 0.07 km/s and $\leq \pm 0.09$ km/s for the Vp and Vs, respectively. The error on the Moho depth is $\leqslant \pm$ 0.450 km.

The ray tracing diagrams (Fig. 8) show a good sampling of all interfaces by P- and S-waves along the whole ALCUDIA-WA transect, except for the southernmost part between 0 and 40 km which is characterized by reduced ray coverage. The phases, often recorded from normal incidence to large offsets (Figs. 3 and 4) constrain the velocities of each interface resulting in a well-resolved crustal model.

The Poisson's ratio is directly related to the elastic properties of the rock, which in turn, depend on the mineral constituents. The Poisson's ratio is also greatly influenced by the fracture network, applied stresses, crack porosity, and voids in a rock mass (Walsh, 1965). Although the seismic velocities are pressure-dependent, its influence on the Poisson's ratio seems to be low on crystalline rocks at a high confining pressure (Christensen, 1996; Wang and Ji, 2009). Poisson's ratio calculations are based on Vp and Vs values, with errors estimated in $\pm$0.07 and $\pm$ 0.15 km/s, respectively. As expected, Poisson's ratio is sensitive to errors in Vp and Vs and its uncertainty depends on the Vp/Vs ratio, given by:

$$\left|\frac{\Delta\sigma}{\sigma}\right| = \frac{2\eta^2}{(\eta^2-1)(\eta^2-2)}\left[\left|\frac{\Delta V_p}{V_p}\right| + \left|\frac{\Delta V_s}{V_s}\right|\right]$$

(Christensen, 1996). Where $\eta = \frac{V_p}{V_s}$. The errors obtained for Vp and Vs imply an uncertainty on the Poisson's ratio of $\leqslant \pm$ 0.025.

6. Discussion

6.1. Crustal composition constraints

Indirect geophysical methods, such as wide-angle seismic modeling, provide a tool to obtain the composition of the inaccessible crust by comparing field physical properties with lab measurements on rock samples. The use of as many available physical properties as possible reduces the range of possible lithologies. By means of the physical properties derived from Vp, Vs, and Poisson's ratio together with a previous density model (Ehsan et al., 2015), we have estimated the composition of the crust of the southern CIZ. In the absence of laboratory studies on rocks and xenoliths of the area, we have used the published laboratory measurements made for the most common crustal rock types (Christensen, 1996; Christensen and Mooney, 1995). These measurements show that seismic velocities are sensitive to temperature and pressure variations, so that an important factor to consider is the thermal gradient of the region. Accordingly, the velocity measurements must be corrected taking into account the effect of the thermal regime in the area. The reported geotherm for western Iberia is of 20 °C/km (Marzán, 2000). Thus, we have considered the values measured on rock samples at high temperature (Christensen and Mooney, 1995). Furthermore, velocities, especially S-wave ones, are strongly influenced by the presence of crack porosity, producing large deviations in the Poisson's ratios. However, crack porosity closes at pressures greater than 100–200 MPa, which corresponds to maximum depths of 6–7 km depth. Accordingly, the influence of crack porosity in our models is expected to affect only the uppermost crust.

The seismic velocity and Poisson's ratio models (Fig. 5) present a clear distinction between the upper and lower crust, as well as lateral variations along the profile. To estimate the composition of the southern

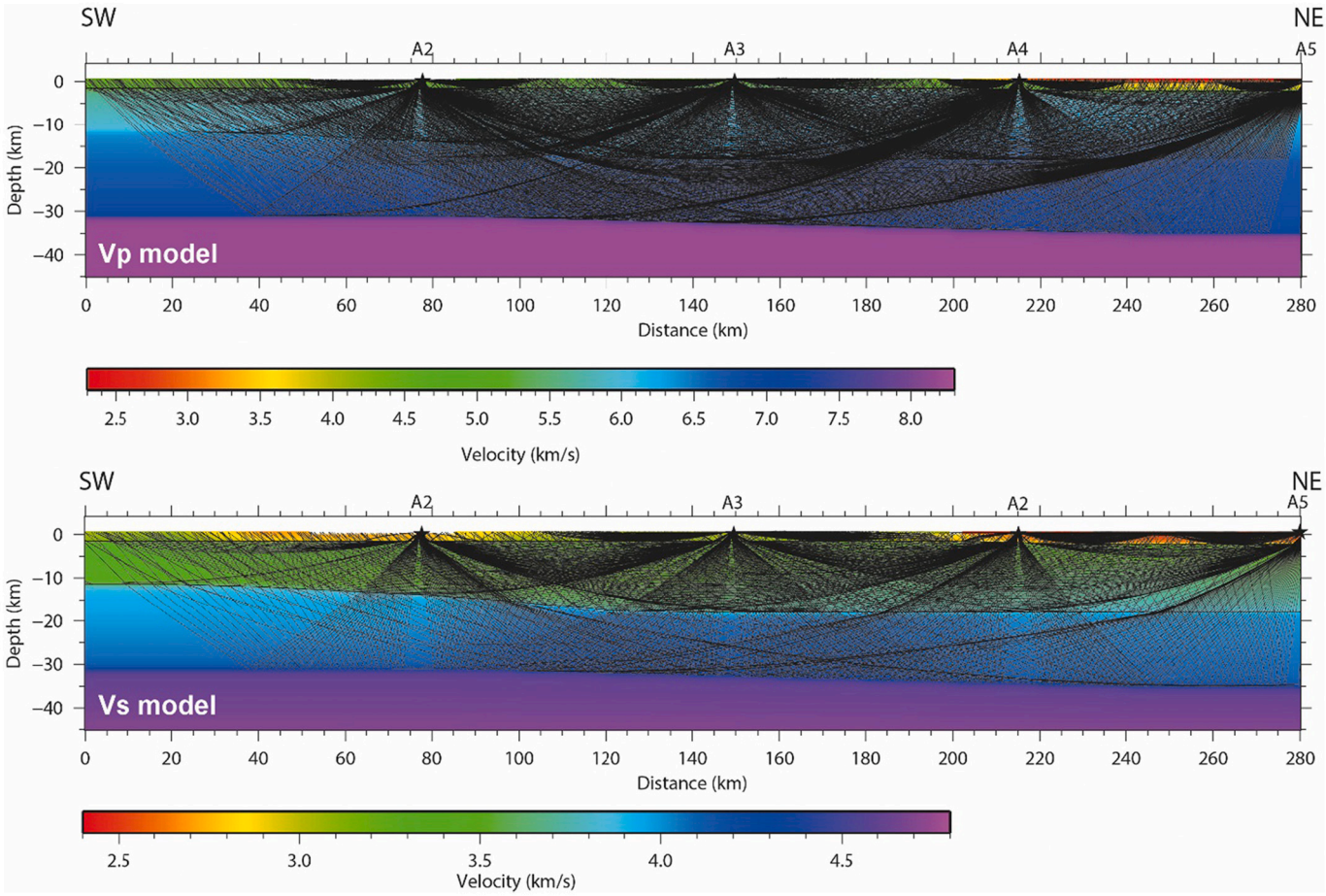

Fig. 8. Raypath coverage (every tenth ray plotted) along the ALCUDIA-WA transect for the P- (top) and S-wave (bottom) phases.

CIZ crust, Vp/depth, Poisson's ratio/depth, and density/depth profiles have been determined by averaging the values from a 20 km-wide strip at different points along the profile: (i) from km 20 to 40, sampling the BCSZ, (ii) from km 120 to 140, sampling the southern CIZ, and (iii) from km 200 to 220, sampling the Mora Batholith and southern TB. Then, a qualitatively smoothing procedure has been applied to the uppermost, upper, and lower crust of the models. The resulting values have been plotted in a comparative chart with the laboratory measurements presented in Table 2 to infer the putative crustal composition. (See Table 3.)

Fig. 9 presents the average Poisson's ratio/Vp and Density/Vp charts along the line. The uppermost crust (0 to ~3–5 km-depth) presents high lateral variability on the P- and S-wave velocities, and, as a result, the Poisson's ratio is also highly variable. The calculated densities for the uppermost crust also vary along the profile with the lowest values in the TB. Despite this variability, the lithology compatible with all the measured physical properties at the southern CIZ crust is a that of metagraywacke, which is one of the dominant outcropping lithologies in that area.

At upper crustal depths, Vp, Vs, and Poisson's ratio vary along the seismic line. Both seismic velocities increase northwards, which, in turn, produces an increase in the Poisson's ratio. In contrast, densities remain constant along the line (Ehsan et al., 2015). The most compatible rock types are granite, gneiss and slate for the southern part of the line, from km 0 to ~150. It is worth noting the Poisson's ratio increase beneath the Pedroches batholith is probably imaging the extension of this pluton at depth. In the northern part of the line, below the Toledo area and TB, the most compatible rock types are gneiss and granite-granodiorite. The increase in the Poisson's ratio denotes a northward change from felsic or siliciclastic to intermediate upper crustal composition. In this respect, the existence of subordinate mafic rocks (La Bastida and Toledo Gabbros) in the Toledo Anatectic Complex (Barbero, 1992; Barbero and Villaseca, 1988), in coincidence with the higher Poisson's ratios observed in the northernmost upper crust (Fig. 4), might suggest the dominance of intermediate igneous rocks at depth.

For the lower crust, Vp and density values are constant along the profile, while Vs values and Poisson's ratios slightly increase and decrease, respectively, northwards. The low Poisson's ratio at these depths might indicate a rather felsic composition for the lower crust beneath the southern CIZ. Interestingly, direct evidence of lower crust composition has been found in the Spanish Central System, north of the northern end of ALCUDIA-WA profile, where Variscan felsic granulites formed in the lower crust appear as xenoliths in Mesozoic dykes (Villaseca et al., 1999). However, the high reflectivity observed in the ALCUDIA vertical incidence seismic profile (Martínez Poyatos et al., 2012) is probably related to the presence of intercalated mafic rocks.

6.2. *Upper crustal structure*

The ALCUDIA experiment crosscuts some important granitic bodies. The Pedroches batholith, a major Late Variscan igneous intrusion, crops out in the southern part of the profile (from km 42 to 50 along the line) (Fig. 1). The ALCUDIA-NI profile imaged this batholith as a transparent body with a lack of internal reflectivity, which soles out at ~4 km-depth (Fig. 5 in Ehsan et al. (2014)). These authors interpret the lack of reflectivity below this depth as the base of the pluton. However, the Poisson's ratio model could suggest that this body could extend deeper downs to the base of the upper crust. Besides the Pedroches batholith, the upper crust of the southern and central parts of the profile is

Table 2
Compressional velocities, Poisson's Ratio (σ) and densities (ρ) for different crustal rock types as function of depth, considering a 20 °C/km thermal gradient. Table modified from Christensen and Mooney (1995) and Christensen (1996).

	5 km			10 km			15 km			20 km			25 km			30 km		
	100 °C			200 °C			300 °C			400 °C			500 °C			600 °C		
	V_p (km/s)	σ	ρ (kg/m^3)	V_p (km/s)	σ	ρ (kg/m^3)	V_p (km/s)	σ	ρ (kg/m^3)	V_p (km/s)	σ	ρ (kg/m^3)	V_p (km/s)	σ σ	ρ (kg/m^3)	V_p (km/s)	σ	ρ (kg/m^3)
Basalt (BAS)	5.84	0.289	2878	5.87	0.290	2883	5.88	0.291	2889	5.88	0.293	2894	5.87	0.294	2899	5.86	0.295	2904
Diabase (DIA)	6.63	0.277	2946	6.64	0.277	2952	6.63	0.278	2957	6.61	0.278	2962	6.58	0.279	2967	6.56	0.279	2973
Granite- Granodiorite (GRA)	6.17	0.236	2654	6.20	0.237	2661	6.20	0.238	2667	6.18	0.239	2673	6.16	0.239	2679	6.13	0.240	2686
Diorite (DIO)	6.40	0.260	2810	6.45	0.261	2815	6.46	0.263	2820	6.45	0.265	2825	6.43	0.266	2831	6.42	0.268	2836
Gabbro- Norite (GAB)	7.04	0.292	2966	7.05	0.293	2971	7.03	0.294	2975	7.01	0.295	2981	6.98	0.295	2985	6.94	0.296	2991
Metagraywacke (MGW)	5.33	0.238	2615	5.44	0.242	2621	5.51	0.245	2627	5.54	0.248	2632	5.57	0.252	2638	5.58	0.255	2644
Slate (SLT)	6.06	0.298	2801	6.09	0.298	2807	6.11	0.297	2813	6.11	0.297	2818	6.11	0.297	2824	6.09	0.297	2830
Phyllite (PHY)	6.07	0.261	2728	6.13	0.262	2734	6.14	0.263	2740	6.13	0.264	2745	6.12	0.265	2751	6.10	0.266	2757
Zeolite facies Basalt (BZE)	6.24	0.293	2916	6.29	0.294	2922	6.31	0.295	2927	6.31	0.297	2932	6.30	0.298	2937	6.28	0.299	2943
Prehnite-Pumpellyite Facies Basalt (BPP)	6.24	0.273	2829	6.30	0.274	2835	6.32	0.276	2840	6.32	0.278	2845	6.31	0.279	2850	6.30	0.281	2856
Greenschist facies Basalt (BGR)	6.64	0.260	2991	6.73	0.260	2996	6.75	0.261	3001	6.74	0.262	3006	6.73	0.263	3012	6.71	0.264	3017
Granite Gneiss (GGN)	5.99	0.243	2662	6.08	0.245	2669	6.09	0.246	2675	6.09	0.248	2681	6.08	0.250	2687	6.07	0.251	2694
Biotite (Tonalite) Gneiss (BGN)	6.09	0.252	2746	6.16	0.253	2753	6.17	0.254	2759	6.17	0.256	2766	6.15	0.257	2772	6.13	0.258	2779
Mica Quartz Schist (QSC)	6.16	0.267	2830	6.26	0.268	2836	6.30	0.269	2843	6.30	0.270	2849	6.29	0.270	2856	6.29	0.271	2862
Amphibolite (AMP)	6.74	0.259	2992	6.81	0.260	2996	6.81	0.261	3001	6.79	0.262	3006	6.76	0.263	3011	6.73	0.264	3016
Felsic Granulite (FGR)	6.30	0.267	2755	6.33	0.268	2761	6.32	0.269	2766	6.30	0.271	2771	6.27	0.272	2776	6.23	0.273	2782
Paragranulite (PGR)	6.23	0.263	2761	6.27	0.264	2766	6.26	0.265	2771	6.24	0.266	2776	6.21	0.266	2782	6.17	0.267	2787
Anorthositic Granulite (AGR)	6.78	0.295	2751	6.81	0.295	2757	6.80	0.296	2762	6.77	0.297	2767	6.74	0.298	2772	6.71	0.299	2778
Mafic Granulite (MGR)	6.74	0.282	2977	6.77	0.282	2983	6.76	0.283	2988	6.73	0.283	2993	6.70	0.283	2998	6.67	0.283	3004
Mafic Garnet Granulite (GGR)	6.97	0.272	3121	7.05	0.273	3127	7.05	0.274	3132	7.04	0.276	3137	7.02	0.277	3142	6.98	0.278	3148
Serpentinite (SER)	5.24	0.342	2571	5.26	0.345	2572	5.25	0.347	2576	5.24	0.350	2579	5.21	0.353	2583	5.18	0.355	2586
Quartzite (QTZ)	5.88	0.072	2646	5.90	0.077	2655	5.88	0.083	2662	5.85	0.088	2669	5.81	0.093	2677	5.77	0.099	2684
Calcite Marble (MBL)	6.80	0.310	2721	6.81	0.306	2725	6.79	0.303	2730	6.76	0.300	2734	6.73	0.296	2739	6.69	0.293	2743
Anorthosite (ANO)	6.85	0.311	2736	6.88	0.311	2739	6.88	0.312	2743	6.86	0.312	2748	6.84	0.312	2752	6.81	0.313	2757
Hornblendite (HBL)	7.05	0.256	3250	7.08	0.256	3252	7.06	0.257	3256	7.03	0.258	3260	7.00	0.259	3264	6.96	0.260	3268
Pyroxenite (PYX)	7.66	0.253	3270	7.67	0.254	3272	7.66	0.255	3276	7.64	0.257	3280	7.61	0.258	3284	7.57	0.259	3288

Table 3
Corresponding P-and S-wave velocities, Poisson's ratio, density, and the proposed rock types beneath the Badajoz-Córdoba Shear Zone, the Central Iberian Zone, and the Tajo Basin, according ours results.

Depth (km)	Vp (km/s)	Vs (km/s)	Poisson's ratio	Density (kg/m^3)	Rock types
Badajoz-Córdoba Shear Zone (from 0 to 40 km along the line)					
0–3	4.50–5.75	2.88–3.35	0.236–0.243	2550–2600	Metagraywacke
3–13	5.8–6.20	3.40–3.90	0.25	2750	Granite gneiss,
13–32	6.4–7.0	3.9–4.1	0.210–0.235	2850–2950	Amphibolite, Greenschist facies basalt
Central Iberian Zone (from 40 to 180 km along the line)					
0–3	5.25–5.75	3.0–3.39	0.245	2600	Metagraywacke
3–17	5.80–6.20	3.4–3.6	0.235–0.240	2750	Granite gneiss,
17–32	6.50–7.00	3.90–4.20	0.205–0.240	2950	Amphibolite, Greenschist facies basalt
Mora Batholith and southern Tajo Basin (from 180 km to the end of the line)					
0–3	4.75–5.8	3.0–3.4	0.20–0.24	2670–2300	Metagraywacke, Sediments
3–18	6.0–6.2	3.5–3.8	0.24–0.26	2750	Granite gneiss, Biotite (tonalite) gneiss, Granite-Granodiorite
18–34	6.7–7.0	4.0–4.2	0.22	2950	Amphibolite, Greenschist facies basalt

characterized by low-grade metasedimentary rocks and a relatively scarce amount of igneous rocks. To the north, the Mora batholith and the Toledo Anatectic complex crop out and define a system of major granitic bodies and high-grade metamorphic rocks (from km 180 to 203 along the line) (Figs. 1 and 5a). The southern boundary of the Toledo Anatectic complex marks the northern limit of the ALCUDIA-NI profile (Martínez Poyatos et al., 2012). Therefore, the continuation of the plutonic and high-grade metamorphic bodies northwards cannot be constrained by that dataset. Nevertheless, the prevailing lithologies cropping out just south and north of the TB (granitoids and migmatites) (Fig. 1) suggest that these lithologies constitute the basement of the Neogene TB too. The modeled upper crustal S- and P-wave velocities (from ~2–15 km-depth) are relatively higher beneath the TB with respect to the rest of the profile (Fig. 5). Likewise, the calculated Poisson's ratio is also higher in this area. The proposed rock types for the upper crust in this area are compatible with the rocks cropping out south and north of the basin (Fig. 1) (migmatites, metapelites, granitoids, and orthogneisses) (e.g. Barbero and Villaseca, 2004; Martínez Poyatos et al., 2004), which are denser and feature a higher metamorphic grade than those exposed to the south (low-grade metasedimentary rocks). According to the field geology and the derived physical property models from the ALCUDIA-WA transect, the most probable lithologies for the upper crust beneath the TB are acidic to intermediate igneous rocks (e.g., granite, granodiorite) and, locally, high-grade metamorphic rocks. Thus, from south to north, an increase in the amount of igneous rocks, in its mafic character and in the grade of metamorphism would explain the increase in velocities and Poisson's ratio within the upper crust beneath the Toledo area and the TB.

6.3. A conspicuous mid-crustal discontinuity

The P- and S-wave velocity models and Poisson's ratios (Fig. 5) reveal a clear interface at ~12 km-depth to the south, which deepens down to ~18 km northwards. This crustal-scale discontinuity has been formerly interpreted to represent the brittle/ductile transition (Ehsan et al., 2015; Simancas et al., 2003). The IBERSEIS and ALCUDIA (Fig. 1) normal incidence datasets (Martínez Poyatos et al., 2012; Simancas et al., 2003) show an upper crust reaching similar depths and featuring a reflectivity pattern that is decoupled from the highly laminated lower crust. In the ALCUDIA-NI profile, the transparent upper crust suggests that the Variscan shortening was homogeneously accommodated by upright folds (Ehsan et al., 2014; Martínez Poyatos et al., 2012). Contrarily, a highly laminated, indicates a long deformed lower crust that in Variscan times has concentrated deformation locally (Ayarza et al., 2020; Simancas et al., 2013). Thus, upper and lower crust reacted differently to shortening, and, hence, a decoupling zone developed at the top of the lower crust (~13–18 km) (Martínez Poyatos et al., 2012). Experiments of layered analog models (Brun, 2002; Burg et al., 1994; Davy and Cobbold, 1991) reproduced similar features.

However, the fact that rocks deformed at ductile conditions crop out above this boundary hinders this interpretation. The new models indicate that this conspicuous boundary, identified across the entire Iberian Massif, represents an orogen scale feature, often acting as a detachment and related to the Conrad discontinuity (Ayarza et al., 2021). Its outstanding signature in this dataset further supports this hypothesis. In fact, in the southern CIZ, the upper to lower crust boundary features a sharp P- and S-wave velocity transition (from 6.2 to 6.6 km/s, and from 3.6 to 3.9 km/s, respectively). This observation probably suggests important changes in the physical properties of the rocks below and above this interface, which does not imply a pressure/temperature boundary as would be expected from the fragile-ductile transition. It is more likely, a lithological and rheological boundary that coincides with the top of the lower crust.

6.4. The lower crust

The lower crust of the southern CIZ (from ~13–20 km down to the Moho) is more homogeneous than the upper crust (Fig. 5), indicating that major crustal variation exists mostly at upper crustal levels. The lower crustal depth and velocity are constrained by the modeling of the PmP and SmS phases. These high amplitude phases are identified from near-normal incidence to offsets larger than 150 km on shot gathers A2-A4 (Figs. 3 and 4), while in shot gather A5 (Fig. 4d), the SmS phase is less prominent at near offsets and reveals relatively weak amplitudes. This shot is placed at the northern border of the Cenozoic TB (Fig. 1). Therefore, the observed decrease in the reflectivity of the SmS phase at near offsets (Fig. 3d) can be explained by S-wave attenuation in the TB, especially in the uppermost 500 m, made up of unconsolidated sediments.

The recorded SmS phase normal incidence travel-time ranges from ~17.5 s to ~19 s, from south to north (Fig. 4). The same variation in intercept time is also identified for the PmP phase, which increases from ~10.5 s to ~11.8 s northwards. This suggests variations in the seismic velocity distribution and/or the crustal thickness along the ALCUDIA-WA transect. Furthermore, the TB also plays an important role. The travel-time variations of Moho reflections are thus explained by: (1) a northward change in the Moho depth; (2) a northward increase in the upper crustal velocities; and (3) the effect of the TB to the north. These three factors together affect travel-times and moveout differences in the crust-mantle reflection phase.

The crust-mantle boundary is located at ~31 km in the southern end of the ALCUDIA-WA profile and ~ 35.5 km in the northern one. Alpine tectonics and/or the orogenic load associated with the Spanish Central System mountain range might explain the smooth increase in crustal thickness northwards. The isostatic response of the crust to denser lithologies may also be responsible for the Moho deepening.

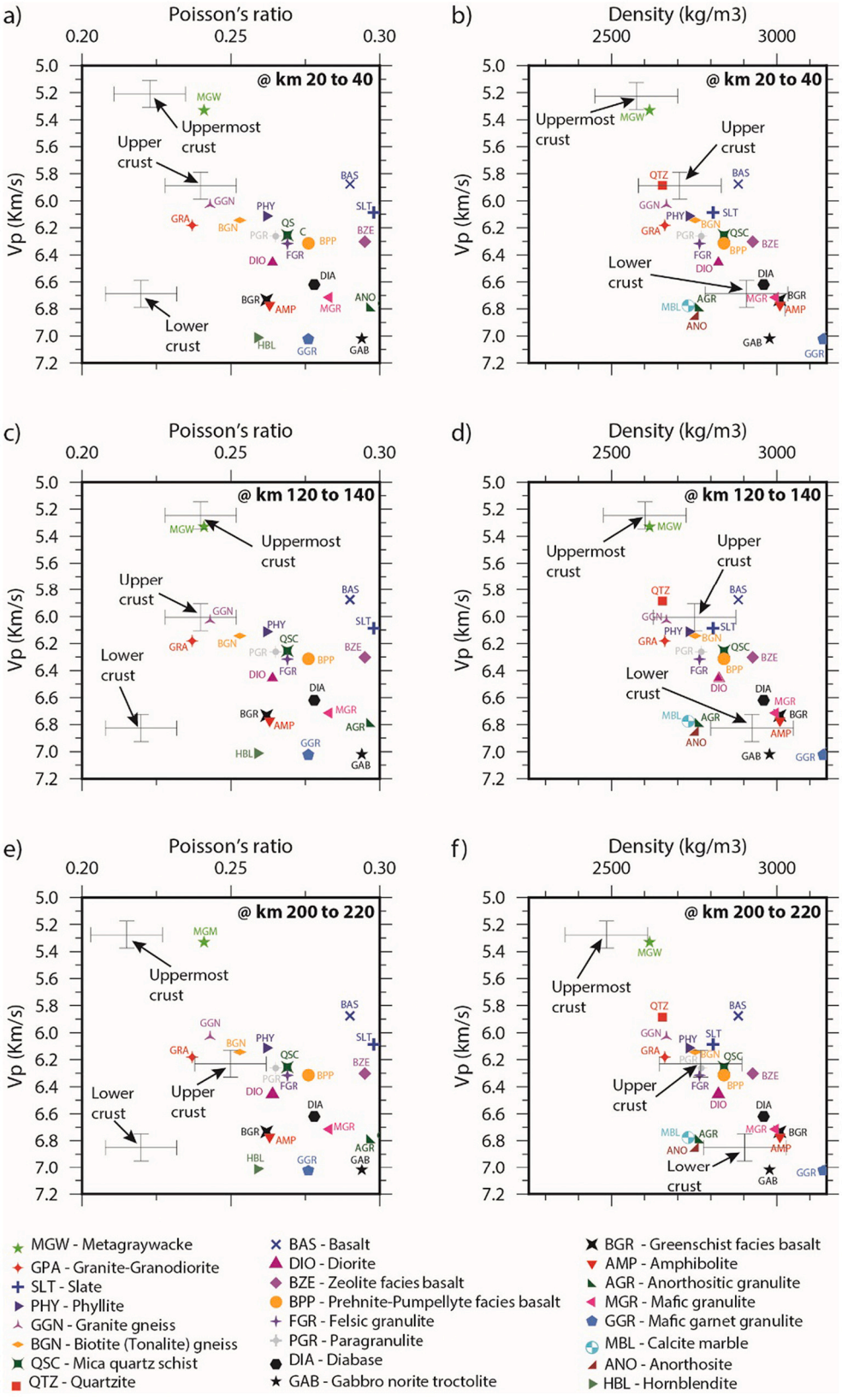

Fig. 9. P-wave velocity versus Poisson's ratio (left panels) and density (right panels) along different points along the ALCUDIA-WA transect compared with rock types listed on Table 2. The values from the ALCUDIA-WA transect are represented by crosses which are indicative of the vertical and horizontal error bars. Density values after Ehsan et al. (2015).

7. Conclusions

The shot gathers of the ALCUDIA-WA transect, acquired over the southern Central Iberian Zone (CIZ), feature high-amplitude P- and S-wave arrivals. The new evaluation of the P-wave arrivals at short offsets resulted in a more detailed P-wave model at shallow depths. Forward modeling of S-wave direct arrivals (Sg) and reflections in the Moho (SmS) allowed us to come up with a ~ 300 km-long crustal S-wave velocity model. From the resulting P- and S-wave velocities we have calculated the Poisson's ratio for the crust of the southern CIZ.

The seismic velocity models show a two-layered crust with conspicuous lateral variations mostly at upper crustal levels. Both, the upper crustal velocity and thickness increase northwards, while the lower crust presents more homogeneous velocities with little increase in S-wave velocities northward. In the same way, the derived Poisson's ratios are predominantly low and show important differences in the crust along the profile. On average, the upper crustal Poisson's ratio values range from 0.23–0.25 within the Badajoz-Córdoba Shear Zone and the southernmost CIZ increasing to ~0.26 below the Mora Batholith and the Tajo Basin (TB). At the lower crust, the Poisson's ratio shows low values of around 0.22.

Based on these variations, the velocity and Poisson's ratio models can be divided into three segments: (i) the BCSZ portion, (ii) the more homogeneous southernmost CIZ, and (iii) the northern portion, ~100 km-long, sampling the Toledo Anatectic Complex and the TB and showing higher heterogeneities.

The composition of the southern CIZ crust is derived from seismic velocities, densities, and Poisson's ratio. In the first part of the profile, the upper crust is dominated by low-grade metasedimentary rocks. Northwards, below the TB, the compositional section suggests the existence of denser rocks. Granitoids and high-grade metasedimentary rocks, which crop out at both margins of the TB, are the probable rocks which underlie the basin. The small variations in seismic velocities and Poisson's ratio values along the lower crust across the southern CIZ indicate no differences at this crustal level. The low Poisson's ratio values in the northernmost segment suggest a mainly felsic composition for the lower crust, although the high reflectivity observed in Normal Incidence data indicates the presence of some mafic intercalations.

A conspicuous upper-lower crust boundary, clearly observed from the resulting S-wave models and formerly identified with normal incidence seismic data (Martínez Poyatos et al., 2012), supports the existence of a major lithological/seismic discontinuity at that level.

The total crustal thickness increases from 31 km-depth in the south to ~35 km-depth at the northern edge of the profile. The deepening of the Moho northwards is probably related to the effect of Alpine tectonics and the isostatic response to the orogenic load of the Spanish CS mountain range.

Declaration of Competing Interest

The authors declare that they have no known competing financial interests or personal relationships that could have appeared to influence the work reported in this paper.

Acknowledgments

The authors thank the Associated Editor and the anonymous reviewers for their thoroughly valuable suggestions and comments that improved the manuscript. Seismic data were collected in 2012 with funding provided by the Spanish Ministry of Science and Innovation (grants: CGL2004-04623/BTE, CGL2007-63101/BTE, CGL2011-24101, CSD2006-00041). Instrumentation was provided by the IRIS-PASSCAL instrument center, Socorro, New Mexico, USA. The seismic data, including experiment geometry are stored in the IRIS-PASSCAL facilities and can be accessed through the IRIS-PASSCAL data management center. I.P. is funded by the Spanish Government and the Universidad de Salamanca with a Beatriz Galindo grant (BEGAL 18/00090). S.A. Ehsan is funded by the European Commission grant Marie Curie Actions (264517-TOPOMOD-FP7-PEOPLE-2010-ITN). We thank Instituto Geológico y Minero de España for providing the logistic help and an academic crew for data acquisition. GMT was used to prepare some of the figures shown in the paper.

The data used in this work is accessible at the DIGITAL.CSIC repository (DeFelipe et al., 2021) at https://doi.org/10.20350/digitalCSIC/9061.

References

Alonso-Zarza, A.M., Calvo, J.P., Silva, P.G., Torres, T., 2004. Cuenca del Tajo. In: Vera, J. A. (Ed.), Geología de España. SGE-IGME, pp. 556–561.

Ayarza, P., Martínez Catalan, J.R., Gallart, J., Pulgar, J.A., Dañobeitia, J.J., 1998. Estudio Sismico de la Corteza Iberica Norte 3.3: a seismic image of the Variscan crust in the hinterland of the NW Iberian Massif. Tectonics 17, 171–186.

Ayarza, P., Martínez Catalán, J.R., Alvarez-Marrón, J., Zeyen, H., Juhlin, C., 2004. Geophysical constraints on the deep structure of a limited ocean-continent subduction zone at the North Iberian Margin. Tectonics 23, TC1010. https://doi.org/10.1029/2002TC001487.

Ayarza, P., Martínez Catalán, J.R., Martínez García, A., Alcalde, J., Andrés, J., Simancas, J.F., Palomeras, I., Martí, D., DeFelipe, I., Juhlin, C., Carbonell, R., 2020. Evolution of the Iberian Massif as deduced from its crustal thickness and geometry of a mid-crustal (Conrad) discontinuity. Solid Earth Discuss. 2020, 1–46. https://doi.org/10.5194/se-2020-158.

Ayarza, P., Martínez Catalán, J.R., Martínez Garciá, A., Alcalde, J., Andrés, J., Simancas, J.F., Palomeras, I., Martí, D., Defelipe, I., Juhlin, C., Carbonell, R., 2021. Evolution of the Iberian Massif as deduced from its crustal thickness and geometry of a mid-crustal (Conrad) discontinuity. Solid Earth 12, 1515–1547. https://doi.org/10.5194/se-12-1515-2021.

Azor, A., González-Lodeiro, F., Simancas, J.F., 1994. Tectonic evolution of the boundary between the Central Iberian and Ossa-Morena zones (Variscan belt, Southwest Spain). Tectonics 13, 45–61.

Azor, A., Dias da Silva, Í., Gómez Barreiro, J., González-Clavijo, E., Martínez Catalán, J. R., Simancas, J.F., Martínez Poyatos, D., Pérez-Cáceres, I., González Lodeiro, F., Expósito, I., Casas, J.M., Clariana, P., García-Sansegundo, J., Margalef, A., 2019. Deformation and structure. In: Quesada, C., Oliveira, J.T. (Eds.), The Geology of Iberia: A Geodynamic Approach. Springer International Publishing, pp. 307–348. https://doi.org/10.1007/978-3-030-10519-8_10.

BABEL Working Group, 1990. Evidence for early proterozoic plate tectonics from seismic reflection profiles in the Baltic Shield. Nature. https://doi.org/10.1038/348034a0.

Barbero, L., 1992. Tres tipos de rocas gabroideas en el complejo de Toledo. Cuad. - Lab. Xeol. Laxe 17, 173–186.

Barbero, L., Villaseca, C., 1988. Gabros coroníticos en el macizo cristalino de Toledo. Geogaceta 5, 66–68.

Barbero, L., Villaseca, C., 2004. El Macizo de Toledo. In: Vera, J.A. (Ed.), Geología de España. SGE-IGME, pp. 110–115.

Birch, F., 1960. The Velocity of Compressional Waves in Rocks to 10 Kilobars, part 1. J. Geophys. Res. 65, 1083–1102. https://doi.org/10.1029/JZ065i004p01083.

Birch, F., 1961. The velocity of compressional waves in rocks to 10 kilobars: 2. J. Geophys. Res. 66, 2199–2224. https://doi.org/10.1029/JZ066i007p02199.

Brun, J.-P., 2002. Deformation of the continental lithosphere: insights from brittle-ductile models. Geol. Soc. London Spec. Publ. 200, 355–370. https://doi.org/10.1144/GSL.SP.2001.200.01.20.

Burg, J.-P., Iglesias, M., Laurent, P., Matte, P., Ribeiro, A., 1981. Variscan intracontinental deformation: the coimbra-cordoba shear zone (SW Iberian Peninsula). Tectonophysics 78, 161–177.

Burg, J.-P., Davy, P., Martinod, J., 1994. Shortening of analogue models of the continental lithosphere: new hypothesis for the formation of the Tibetan plateau. Tectonics 13, 475–483. https://doi.org/10.1029/93TC02738.

Carbonell, R., 2004. On the nature of mantle heterogeneities and discontinuities: evidence from a very dense wide-angle shot record. Tectonophysics 388, 103–117. https://doi.org/10.1016/j.tecto.2004.07.025.

Carbonell, R., Gallart, J., Pérez-Estaún, A., Diaz, J., Kashubin, S., Mechie, J., Wenzel, F., Knapp, J.H., 2000. Seismic wide-angle constraints on the crust of the southern Urals. J. Geophys. Res. 105, 13755–13777. https://doi.org/10.1029/2000JB900048.

Christensen, N.I., 1996. Poisson ' s ratio and crustal seismology. J. Geophys. Res. 101, 3139–3156.

Christensen, N.I., Mooney, W.D., 1995. Seismic velocity structure and composition of the continental crust: a global view. J. Geophys. Res. 100, 9761–9788.

Cook, F.A., Van Der Velden, A.J., Hall, K.W., Roberts, B.J., 1999. Frozen subduction in Canada's Northwest Territories: Lithoprobe deep lithospheric reflection profiling of the western Canadian Shield. Tectonics 18, 1–24. https://doi.org/10.1029/1998TC900016.

Cook, F.A., Clowes, R.M., Snyder, D.B., van der Velden, A.J., Hall, K.W., Erdmer, P., Evenchick, C.A., 2004. Precambrian crust beneath the Mesozoic northern Canadian Cordillera discovered by Lithoprobe seismic reflection profiling. Tectonics 23, 1–28. https://doi.org/10.1029/2002TC001412.

Davy, P., Cobbold, P.R., 1991. Experiments on shortening of a 4-layer model of the continental lithosphere. Tectonophysics 188, 1–25. https://doi.org/10.1016/0040-1951(91)90311-F.

de Vicente, G., Muñoz-Martín, A., 2013. The Madrid Basin and the Central System: a tectonostratigraphic analysis from 2D seismic lines. Tectonophysics 602, 259–285. https://doi.org/10.1016/j.tecto.2012.04.003.

DeFelipe, I., Alcalde, J., Ivandic, M., Martí, D., Ruiz, M., Marzán, I., Diaz, J., Ayarza, P., Palomeras, I., Fernandez-Turiel, J.L., Molina, C., Bernal, I., Brown, L., Roberts, R., Carbonell, R., 2021. Reassessing the lithosphere: SeisDARE, an open-access seismic data repository. Earth Syst. Sci. Data 13, 1053–1071. https://doi.org/10.5194/essd-13-1053-2021.

Ehsan, S.A., Carbonell, R., Ayarza, P., Martí, D., Pérez-Estaún, A., Martínez-Poyatos, D.J., Simancas, J.F., Azor, A., Mansilla, L., 2014. Crustal deformation styles along the reprocessed deep seismic reflection transect of the Central Iberian Zone (Iberian Peninsula). Tectonophysics 621, 159–174. https://doi.org/10.1016/j.tecto.2014.02.014.

Ehsan, S.A., Carbonell, R., Ayarza, P., Martí, D., Martínez Poyatos, D., Simancas, J.F., Azor, A., Ayala, C., Torné, M., Pérez-Estaún, A., 2015. Lithospheric velocity model across the Southern Central Iberian Zone (Variscan Iberian Massif): the ALCUDIA wide-angle seismic reflection transect. Tectonics 34, 535–554. https://doi.org/10.1002/2014TC003661.

Flecha, I., Palomeras, I., Carbonell, R., Simancas, F., Ayarza, P., Matas, J., González-Lodeiro, F., Pérez-Estaún, A., 2009. Seismic imaging and modelling of the lithosphere of SW-Iberia. Tectonophysics 472, 148–157. https://doi.org/10.1016/j.tecto.2008.05.033.

Franke, W., 2000. The mid-European segment of the Variscides: tectonostratigraphic units, terrane boundaries and plate tectonic evolution. Geol. Soc. London Spec. Publ. 179, 35–61. https://doi.org/10.1144/GSL.SP.2000.179.01.05.

García-Lobón, J.L., Rey-Moral, C., Ayala, C., Martín-Parra, L.M., Matas, J., Reguera, M.I., 2014. Regional structure of the southern segment of Central Iberian Zone (Spanish Variscan Belt) interpreted from potential field images and 2.5 D modelling of Alcudia gravity transect. Tectonophysics 614, 185–202. https://doi.org/10.1016/j.tecto.2013.12.005.

Gómez-Pugnaire, M.T., Azor, A., Fernández-Soler, J.M., López Sánchez-Vizcaíno, V., 2003. The amphibolites from the Ossa-Morena/Central Iberian Variscan suture (Southwestern Iberian Massif): geochemistry and tectonic interpretation. Lithos 68, 23–42. https://doi.org/10.1016/S0024-4937(03)00018-5.

Hawman, R.B., Colburn, R.H., Walker, D.A., Smithson, S.B., 1990. Processing and inversion of refraction and wide-angle reflection data from the 1986 Nevada PASSCAL experiment. J. Geophys. Res. 95, 4657–4691. https://doi.org/10.1029/JB095iB04p04657.

Iliha DSS Group, 1993. A deep seismic sounding investigation of lithospheric heterogeneity and anisotropy beneath the Iberian Peninsula. Tectonophysics 221, 35–51.

Knapp, J.H., Steer, D.N., Brown, L.D., Berzin, R., Suleimanov, A., Stiller, M., Luschen, E., Brown, D.L., Bulgakov, R., Kashubin, S.N., Rybalka, A.V., 1996. Lithosphere-scale seismic image of the southern urals from explosion-source reflection profiling. Science (80-.). 274, 226–228. https://doi.org/10.1126/science.274.5285.226.

López Sánchez-Vizcaíno, V., Gómez-Pugnaire, M.T., Azor, A., Fernández-Soler, J.M., 2003. Phase diagram sections applied to amphibolites: a case study from the Ossa-Morena/Central Iberian Variscan suture (Southwestern Iberian Massif). Lithos 68, 1–21. https://doi.org/10.1016/S0024-4937(03)00017-3.

Martínez Catalán, J.R., Martínez Poyatos, D., Fea, F., 2004. Zona Centroibérica. In: Vera, J.A. (Ed.), Geología de España. SGE-IGME, pp. 68–133.

Martínez Poyatos, D., Gutiérrez Marco, J.C., Prado Alonzo, M.V., Rábano, I., Sarmiento, G.N., 2004. La Secuencia Paleozoica postcámbrica. In: Vera, J.A. (Ed.), Geología de España. SGE-IGME, pp. 81–83.

Martínez Poyatos, D., Carbonell, R., Palomeras, I., Simancas, J.F., Ayarza, P., Martí, D., Azor, A., Jabaloy, A., González Cuadra, P., Tejero, R., Martín Parra, L.M., Matas, J., González Lodeiro, F., Pérez-Estaún, A., García Lobón, J.L., Mansilla, L., 2012. Imaging the crustal structure of the Central Iberian Zone (Variscan Belt): the ALCUDIA deep seismic reflection transect. Tectonics 31, TC3017. https://doi.org/10.1029/2011TC002995.

Marzán, I., 2000. Régimen térmico de la Península Ibérica. Estructura litoférica a través del Macizo Ibérico y el margen Subportugués. University of Barcelona, Spain.

Matte, P., 1986. Tectonic and plate tectonics model for the Variscan belt of Europe. Tectonophysics 126, 329–374.

Matte, P., 2001. The Variscan collage and orogeny (480-290 Ma) and the tectonic definition of the Armorica microplate: a review. Terra Nova 13, 122–128.

MONA LISA Working Group, 1997. MONA LISA - deep seismic investigations of the lithosphere in the southeastern North Sea. Tectonophysics 269, 1–19. https://doi.org/10.1016/S0040-1951(96)00111-4.

Monteiro Santos, F.A., Pous, J., Almeida, E.P., Queralt, P., Marcuello, A., Matias, H., Victor, L.A.M., 1999. Magnetotelluric survey of the electrical conductivity of the crust across the Ossa Morena Zone and South Portuguese Zone suture. Tectonophysics 313, 449–462. https://doi.org/10.1016/S0040-1951(99)00209-7.

Ordoñez Casado, B., 1998. Geochronological Studies of the Pre-Mesozoic Basement of the Iberian Massif: The Ossa-Morena and the Allochthonous Complexes within the Central Iberian Zone (ETH.).

Palomeras, I., Carbonell, R., Flecha, I., Simancas, F., Ayarza, P., Matas, J., Poyatos, D.M., Azor, A., Lodeiro, F.G., Pérez-Estaun, A., 2009. Nature of the lithosphere across the Variscan orogen of SW Iberia: Dense wide-angle seismic reflection data. J. Geophys. Res. Solid Earth 114, B02302. https://doi.org/10.1029/2007JB005050.

Palomeras, I., Carbonell, R., Ayarza, P., Martí, D., Brown, D., Simancas, J.F., 2011. Shear wave modeling and Poisson's ratio in the Variscan Belt of SW Iberia. Geochem. Geophys. Geosyst. 12 https://doi.org/10.1029/2011GC003577 n/a-n/a.

Pérez-Estaún, A., Bea, F., 2004. Macizo Ibérico. In: Vera, J.A. (Ed.), GEOLOGÍA DE ESPAÑA. SGE-IGME, Madrid, pp. 21–230.

Pous, J., Muñoz, G., Heise, W., Melgarejo, J.C., Quesada, C., 2004. Electromagnetic imaging of Variscan crustal structures in SW Iberia: the role of interconnected graphite. Earth Planet. Sci. Lett. 217, 435–450. https://doi.org/10.1016/S0012-821X(03)00612-5.

Pous, J., Martínez Poyatos, D., Heise, W., Santos, F.M., Galindo-Zaldívar, J., Ibarra, P., Pedrera, A., Ruiz-Constán, A., Anahnah, F., Gonçalves, R., Mateus, A., 2011. Constraints on the crustal structure of the internal Variscan Belt in SW Europe: a magnetotelluric transect along the eastern part of Central Iberian Zone, Iberian Massif. J. Geophys. Res. Solid Earth 116, 1–20. https://doi.org/10.1029/2010JB007538.

Rudnick, R.L., Fountain, D.M., 1995. Nature and composition of the continental crust: a lower-crustal perspective. Rev. Geophys. 33, 267–309. https://doi.org/10.1029/95rg01302.

Ruiz, M., Díaz, J., Pedreira, D., Gallart, J., Pulgar, J.A., 2017. Crustal structure of the North Iberian continental margin from seismic refraction/wide-angle reflection profiles. Tectonophysics 717, 65–82. https://doi.org/10.1016/j.tecto.2017.07.008.

Shillington, D.J., Van Avendonk, H.J.A., Holbrook, W.S., Kelemen, P.B., Hornbach, M.J., 2004. Composition and structure of the central Aleutian island arc from arc-parallel wide-angle seismic data. Geochem. Geophys. Geosyst. 5 https://doi.org/10.1029/2004GC000715.

Simancas, J.F., 2019. Variscan cycle. In: Quesada, C., Oliveira, J.T. (Eds.), The Geology of Iberia: A Geodynamic Approach, pp. 1–25. https://doi.org/10.1007/978-3-030-10519-8_1.

Simancas, J.F., Martinez Poyatos, D., Exposito, I., Azor, A., Gonzalez-Lodeiro, F., 2001. The structure of a major suture zone in the SW Iberian Massif: the Ossa-Morena/Central Iberian contact. Tectonophysics 332, 295–308.

Simancas, J.F., Carbonell, R., González-Lodeiro, F., Pérez-Estaún, A., Juhlin, C., Ayarza, P., Kashubin, A., Azor, A., Martínez Poyatos, D., Almodovar, G.R., Pascual, E., Saez, R., Exposito, I., 2003. Crustal structure of the transpressional Variscan orogen of SW Iberia: SW Iberia deep seismic reflection profile (IBERSEIS). Tectonics 22, 1062. https://doi.org/10.1029/2002TC001479.

Simancas, J.F., Ayarza, P., Azor, A., Carbonell, R., Martínez Poyatos, D., Pérez-Estaún, A., González Lodeiro, F., 2013. A seismic geotraverse across the Iberian Variscides: Orogenic shortening, collisional magmatism, and orocline development. Tectonics 32, 417–432. https://doi.org/10.1002/tect.20035.

Villaseca, C., Downes, H., Pin, C., Barbero, L., 1999. Nature and composition of the lower continental crust in Central Spain and the granulite-granite linkage: inferences from granulitic xenoliths. J. Petrol. 40, 1465–1496. https://doi.org/10.1093/petroj/40.10.1465.

Walsh, J.B., 1965. The effect of cracks in rocks on poisson's ratio. J. Geophys. Res. 70.

Wang, Q., Ji, S., 2009. Poisson's ratios of crystalline rocks as a function of hydrostatic confining pressure. J. Geophys. Res. Solid Earth 114. https://doi.org/10.1029/2008JB006167.

Zelt, C.A., Smith, R.B., 1992. Seismic traveltime inversion for 2-D crustal velocity structure. Geophys. J. Int. 108, 16–34.

Zhao, B., Zhang, Zhi, Bai, Z., Badal, J., Zhang, Zhongjie, 2013. Shear velocity and Vp/Vs ratio structure of the crust beneath the southern margin of South China continent. J. Asian Earth Sci. 62, 167–179. https://doi.org/10.1016/j.jseaes.2012.08.013.